THE UNIVERSITY OF MICHIGAN RESEARCH INSTITUTE
ANN ARBOR

ANALYSIS OF A CLASS OF SELF-BIASED OSCILLATORS

Technical Report No. 100
2899-17-T

Cooley Electronics Laboratory
Department of Electrical Engineering

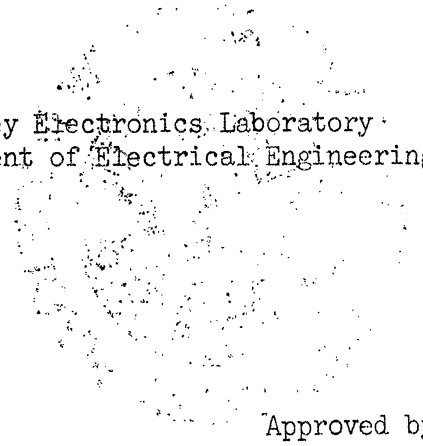

By: F. N. Bailey
A. W. Naylor

Approved by: A. B. Macnee

Project 2899

TASK ORDER NO. CEL-1
CONTRACT NO. DA-36-039 sc-78283
SIGNAL CORPS, DEPARTMENT OF THE ARMY
DEPARIMENT OF ARMY PROJECT NO. 3A99-06-001-01

January 1961

ERRATA

Technical Report No. 100

Page

13 Line 11:

"$a_c(e_c)$ = pentode current..."

should read:

"$a_c(e_c)$ = pentode grid current..."

17 Line 6:

"$e_c(t)$ [$e_c(t)$ = $E_c(t)$ +..."

should read:

"$e_c(t)$ [recall that $e_c(t)$ = $E_c(t)$ +..."

34 Line 9

"...are indicated by vectors."

should read:

"...is indicated by vectors."

41 Line 8:

"outside L_1 also result..."

should read:

"outside L_1 (except those on the E_c axis) also result..."

46 Line 14:

"G_g = 1000 pf"

should read:

"C_g = 1000 pf"

57 Line 5 from bottom:

"mode is altered."

should read:

"modes is altered."

70 Line 14:

"...amplitude mode..."

should read:

"...amplitude-modulated mode..."

ERRATA (continued)

Technical Report No. 100

Page

73 Line 13:

"E_c in the region..."

should read:

"E_c and satisfy a Lipschitz condition in the region..."

77 Line 4 from bottom:

"S > R]."

should read:

"B > R]."

43 Fig. 4.5(b):

"20 μsec/cm" and "8 v/cm"

should read:

"22 μsec/inch" and "8.8 v/inch," respectively.

[Note that the horizontal line below the t axis corresponds to $e_c = -8v$.]

In all figures [except Fig. 4.5(b), noted above] where the scale is given as "v/cm" or "μsec/cm," change "cm" to "side of smallest square."

engn
JMR0172

TABLE OF CONTENTS

LIST OF ILLUSTRATIONS

List of Illustrations (cont'd)

List of Illustrations (cont'd)

LIST OF SYMBOLS

ABSTRACT

One of the classical mathematical models for the self-excited oscillator has been the van der Pol equation. However, this model does not display several modes of behavior frequently observed in simple oscillators. This report presents a method for analyzing a self-excited oscillator which does exhibit several modes of behavior. The methods employed, although quite general, are applied in detail to the analysis of a circuit having much in common with a large number of class-C oscillators.

In the circuit chosen the tube has been replaced by two nonlinear conductances representing grid and plate conduction. The resulting mathematical description consists of a system of three first-order, ordinary differential equations. By employing the method of Kryloff and Bogoliuboff, another, more tractable, system of differential equations is determined as an approximation to the original system. This approximating system is found to be second order and amenable to solution by standard phase-plane techniques. The phase-plane solution of the approximating system results in three configurations of limit cycles and equilibrium points characteristic of three frequently encountered modes of self-excited oscillator behavior (i.e., CW, amplitude-modulated, and squegging). A qualitative relationship between the oscillator circuit parameters and phase-plane configurations is then established allowing the prediction of the behavior of a specific oscillator as one of its parameters is varied. It is also found that bistable operation may occur.

These results are checked against the performance of an experimental oscillator. The actual performance of the oscillator is shown to correspond quite closely to the predicted behavior. The several phase-plane configurations, the variation in behavior as a parameter is varied, and the bistable operation all occur as predicted suggesting the probable validity of the mathematical model and giving considerable insight into self-biased oscillator operation.

ANALYSIS OF A CLASS OF SELF-BIASED OSCILLATORS

1. INTRODUCTION

It is the purpose of this report to present a method for analyzing a self-excited oscillating circuit which exhibits several modes of oscillation. The particular oscillator which is analyzed is of special interest because it has much in common with a large number of class-C oscillators. Consequently, it is possible to infer a great deal regarding the behavior of any one of these oscillators from the behavior of the specific oscillator treated in this report. Moreover, the analytic methods employed in this report can be adopted for the analysis of many other oscillators or nonlinear circuits.

It is well known that the analysis of self-excited oscillating circuits presents formidable difficulties. These difficulties arise from the inherently nonlinear character of such circuits. For example, the plate and grid currents of a pentode as functions of grid voltage are two nonlinear functions which arise often in such circuits. As a consequence of the nonlinear character of these circuits, their mathematical characterization must involve nonlinear differential equations and, perhaps, even nonlinear difference-differential equations. Unfortunately, it is seldom the case that these mathematical characterizations can be both reasonably identifiable with the physical system and easily integrated. The usual problem is that if the mathematical characterization adheres closely to the physical system then the nonlinear differential equations are depressingly difficult to handle. Conversely,

if the mathematical characterization is overly simplified, important aspects of the physical system's behavior do not appear in the analytical results. Moreover, even in the case where a satisfactorily simple mathematical characterization has been found it usually happens that exact solutions of the resulting nonlinear equation cannot be readily determined, and some approximation technique must be employed. Thus, two approximations are involved: (1) in the selection of the equation, and (2) in its solution. Clearly, then, the analysis of self-excited oscillating circuits demands a suitable compromise to this mathematical characterization problem.

One of the classic solutions to the above compromise problem is the use of the van der Pol equation as a mathematical characterization of a CW oscillator [Ref. 1]. Although it cannot be questioned that this use of the van der Pol equation has given powerful insight into the operation of CW oscillators, it is also true that it does not lead to an understanding of many phenomena which are observed in oscillators, e.g., nonsinusoidal oscillations. In order to appreciate why this is true it is merely necessary to recall the assumptions which must be made so that the van der Pol equation can be employed. Some of these are that (1) no grid current flows, (2) the grid bias is supplied from a regulated source, (3) the linear feedback network around the tube is a simple parallel resonant tank circuit, (4) the only possible stable oscillation is well approximated by a sinusoidal function,[1] and (5) the

[1] It is not true that the van der Pol equation has a sinusoidal solution. However, the first approximation to the periodic solution is a sinusoidal function. It is this approximation that is usually assumed in characterizing the oscillation of a van der Pol oscillator. It should also be added that the van der Pol equation is a suitable mathematical characterization for the "build up" of oscillation in some oscillators.

plate current as a function of grid voltage is well approximated by a linear plus a cubic term in the grid voltage.

It is clear that assumptions (1) and (2), particularly in the case of an oscillator with grid-leak type bias, are not likely to apply to the experimental situation. Furthermore, it is possible for relatively simple oscillators to exhibit nonsinusoidal and aperiodic oscillations; therefore, assumption (4) without doubt limits the applicability of the van der Pol equation. Assumption (3) guarantees that the nonlinear differential equation which characterizes the oscillator is second order whether it is the van der Pol equation or not. Obviously this limitation to a second-order equation is desirable from a mathematical point of view, but it is also obviously not completely realistic from a physical point of view. There are, usually, parameters that must be neglected before a second-order equation can be attained. Assumption (5) is justified as long as the operating point of the oscillator is constant. On the other hand, in the case of squegging oscillators, which are treated in this report, this assumption does not lead to a realistic representation of the plate current as a function of grid voltage.

It can be seen, then, that the use of the van der Pol equation involves quite a number of restrictive assumptions. Since there are simple experimental oscillators which exhibit considerably different modes of oscillation from those predicted by the van der Pol equation, it is reasonable to attempt to eliminate or alter the above assumptions so that a new mathematical model can be obtained which exhibits these other modes. It is manifest that this new mathematical model should be as simple as possible; moreover, it should be of a form amenable to solution by known methods. Otherwise it will be a poor solution to the

compromise problem which was mentioned previously.

In this report a mathematical model is selected which exhibits some of the oscillation modes that are often associated with a grid-leak biased oscillator. The oscillation modes of interest are (1) CW oscillation, (2) amplitude-modulating, (3) self-pulsing or squegging, and (4) multimode operation. The last term refers to the possibility of more than one stable mode of oscillation for a given set of circuit parameters.

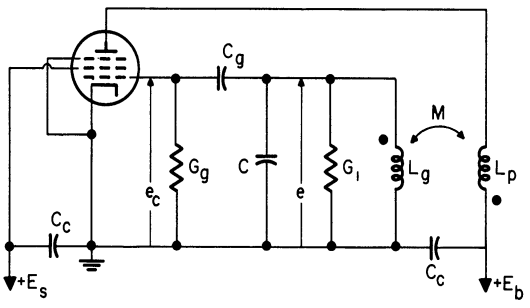

Fig. 1.1. Oscillator circuit.

This mathematical model is developed from a consideration of the circuit shown in Fig. 1.1. Note that this circuit is very similar to the circuit usually associated with the van der Pol oscillator [Ref. 1]. However, there are differences between this circuit and the van der Pol oscillator which are sufficient to make the present circuit considerably more general than the van der Pol circuit. The obvious difference is the addition of the RC grid-leak circuit between the tank circuit and the grid. Beyond this it is assumed that grid current can flow. Although the analytic methods which will be employed are applicable to a more or less arbitrary grid characteristic, the specific example worked out in detail in this paper is based on the assumption that the grid current versus grid voltage is as shown in Fig. 1.2. Similarly, the plate current versus grid voltage characteristic assumed in the detailed example is as shown in Fig. 1.3, even though the analytical techniques apply to a more or less arbitrary plate characteristic.

This choice for the plate current characteristic allows varying operating points to be handled realistically, and should be contrasted with $a_1(e_c) = I_o + c_1 e_c - c_2 e_c^3$ which[1] is assumed for the van der Pol oscillator. It is shown below that the circuit in Fig. 1.1 requires a third-order nonlinear differential equation for its characterization as opposed to the second-order van der Pol equation.

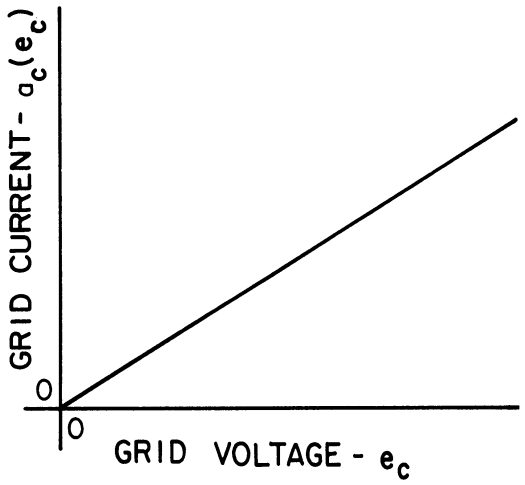

Fig. 1.2. Grid-current characteristic.

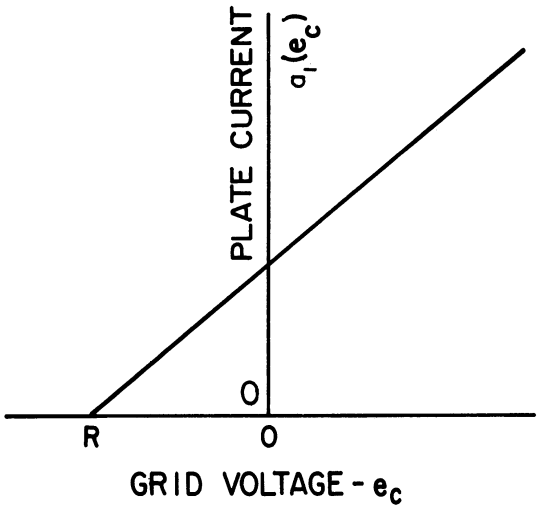

Fig. 1.3. Plate-current characteristic.

It is apparent that this circuit along with the assumptions regarding the characteristics of its elements is representative of a large class of oscillators.

Before analyzing the circuit shown in Fig. 1.1, it is worthwhile to consider a qualitative discussion of its modes of operation. In the case of the CW or constant amplitude mode of oscillation the grid voltage, e_c, is well approximated by

$$e_c(t) = E_c + E \cos(\omega t + \theta) , \qquad (1.1)$$

where E_c, a constant, is the grid bias voltage developed across the grid leak capacitance, C_g, and E is the amplitude of CW oscillation measured

[1] The symbol "a" is used for current to avoid the confusing symbol for the derivative of "i" in the dot notation ($dx/dt = \dot{x}$) to be used later.

at the tank circuit. The grid bias voltage arises from the pulse of grid current which occurs during each cycle of oscillation (i.e., when $e_c > 0$) and replenishes the charge on C_g. The constant amplitude mode results when over one cycle of oscillation the charge added to C_g during grid conduction is just equal to the charge lost by discharge through the conductance G_g. For such a mode to exist as a steady state behavior, it is necessary, of course, that it be stable. That is, any disturbance away from this equilibrium should decay over a number of cycles instead of growing. In other words, if this mode of oscillation is unstable it will not be observed experimentally even though it is mathematically possible.

If the CW or constant amplitude mode of oscillation is unstable, the oscillator may take up some other mode of oscillation which is stable. For example, imagine the neighborhood of an unstable CW mode as a starting point. The grid voltage is now represented by

$$e_c(t) = E_c(t) + E(t) \cos(\omega t + \theta) . \qquad (1.2)$$

Since the CW mode is unstable, $E_c(t)$ does not approach the constant E_c of Eq. 1.1 as $t \to \infty$ nor does $E(t)$ approach the constant E of the same equation. Instead, as is shown later in this report, they may approach a closed operating path in the (E, E_c)-plane. Such operating paths, similar to the one illustrated in Fig. 1.4, are common to several modes of oscillator operation (e.g., amplitude modulated and

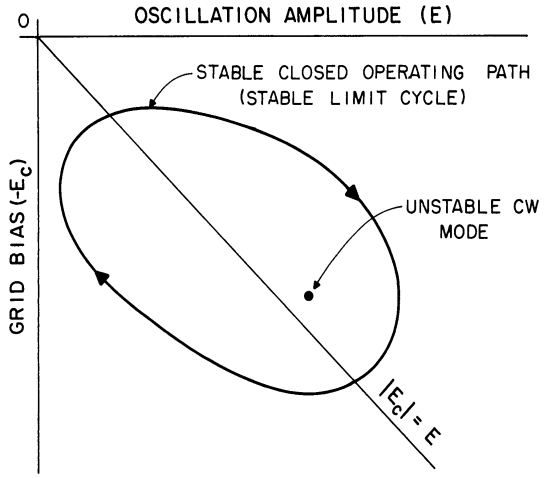

Fig. 1.4. Illustration of a stable closed operating path or limit cycle.

squegging). It can be seen that the operating path in Fig. 1.4 corresponds to a grid voltage which is an amplitude-modulated waveform superimposed upon a periodically varying bias level. A typical grid voltage waveform for this mode is shown in Fig. 1.5.

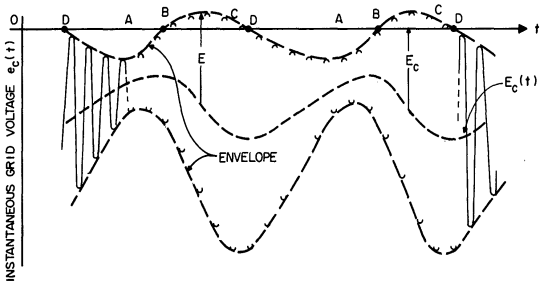

Fig. 1.5. Example of amplitude-modulated oscillation.

In order to appreciate the operation of the oscillator in this mode, it is necessary to note that the "average g_m" (this concept is made precise later in this report) of the tube is a function of both E and E_c. For the specific plate-current characteristic shown in Fig. 1.3 it can be seen that the small-signal g_m for the tube is as shown in Fig. 1.6. This small signal g_m is, of course, the limit of the "average g_m" as $E \to 0$. The complete behavior of the "average g_m" as a function of E and E_c (again assuming the plate characteristic of Fig. 1.3) is depicted in Fig. 1.7. For certain regions of the (E, E_c)-plane the "average g_m" is above some critical level which is associated with a "loop gain of one"; consequently, E(t) is an increasing function of t in those regions.

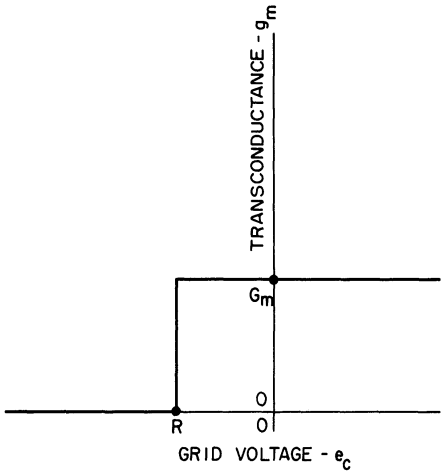

Fig. 1.6. Small-signal g_m.

In the remainder of the (E, E_c)-plane, E(t) is a decreasing function of t. Now consider the oscillation shown in Fig. 1.5 and its associated

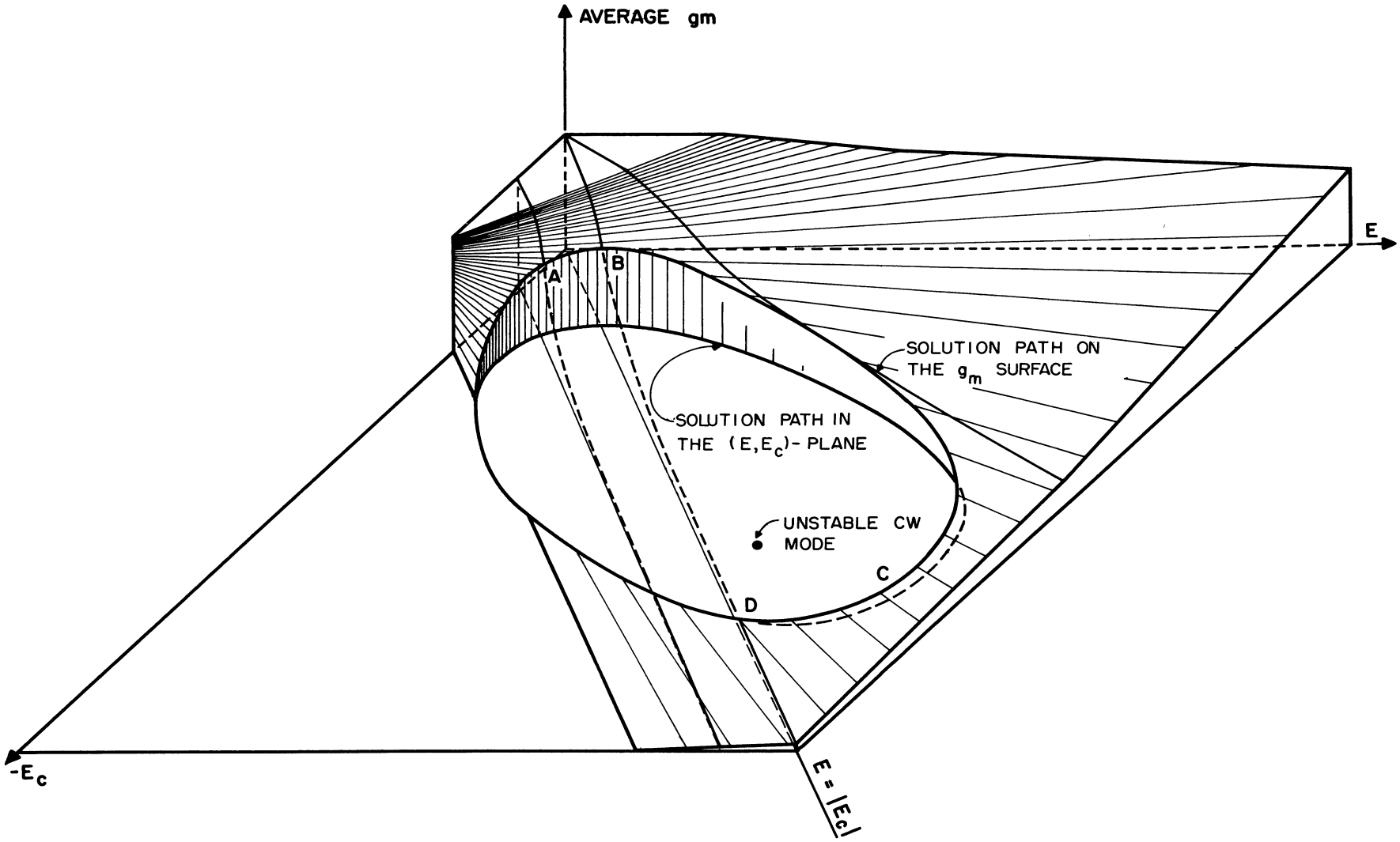

Fig. 1.7. "Average g_m" over the (E, E_c)-plane. The operating path and the points A, B, C, and D correspond to the waveform and points in Fig. 1.5.

operating path on the "average g_m" surface shown in Fig. 1.7. Imagine that at point A in Figs. 1.5 and 1.7 the values of E and E_c correspond to an "average g_m" which is slightly larger than the critical "average g_m". The amplitude of oscillation, E(t), must be an increasing function of t at this point. Moreover, because grid current is not flowing, the grid leak capacitor, C_g, must be discharging; consequently, the bias voltage $E_c(t)$ must be increasing toward zero. However, at point B grid current begins to flow. Shortly after point B the charge added to C_g each cycle by grid conduction becomes greater than the charge lost through the grid leak resistor G_g; consequently, the grid bias, $E_c(t)$, goes through a maximum and starts to decrease. Since the "average g_m" is still above the critical level in the corresponding region of the (E, E_c)-plane (see operating path in Fig. 1.7), E(t) continues to increase while $E_c(t)$ decreases. However, it can be seen from Fig. 1.7 that as $E_c(t)$ becomes more negative the "average g_m" begins to drop off and eventually at point C it becomes less than the critical level. At this point E(t) starts to decrease. At point D, E(t) has become so small that no grid current flows; therefore, at this point $E_c(t)$ begins to increase toward zero again. If the circuit parameters are properly selected, E(t) will decrease more rapidly than $E_c(t)$ increases, and $E_c(t)$ will not be able to "catch up" with E(t) until the E and E_c corresponding to point B are reached. This locus of E, E_c points in the (E, E_c)-plane describes an amplitude-modulation mode operating path of the oscillator.

Note that in the foregoing discussion the effect of grid conduction upon the loop gain has been ignored. Obviously, it reduces the loop gain as grid current flows over a larger and larger portion of

the RF cycle. This effect is not neglected in the analysis which follows.

As the rate at which $E_c(t)$ increases after point C becomes smaller and smaller, the amplitude-modulated mode transforms into another closed operating path mode, that is, the squegging mode. The (E, E_c)-plane operating path for a squegging mode is shown in Fig. 1.8. It is clear that such an operating path will lead to an E(t) which is small for a major portion of its period; i.e., the RF will appear in pulses. Merely on the basis of Fig. 1.8 there does not appear to be a fundamental difference between the squegging mode and the amplitude-modulated mode. However, there is a significant distinction between them. In the case of the amplitude-modulated mode the entire oscillation is deterministic. On the other hand, it is assumed that in the squegging mode E(t) becomes so small between pulses that it is dominated by circuit noise. Consequently, each pulse is initiated by a noise voltage instead of the remnants of the preceding pulse. It follows that in the case of the squegging mode the oscillation is not deterministic, rather it is stochastic. The pulse spacing will be a random variable about some mean value; the phase of each pulse will be a random variable; pulse heights will vary, and so on[1].

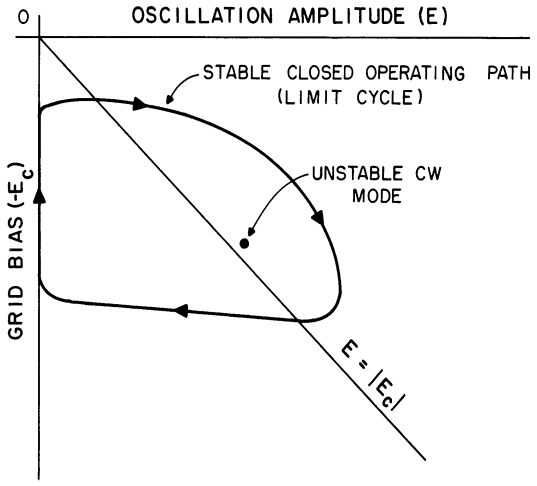

Fig. 1.8. Illustration of a typical squegging-mode operating path or limit cycle.

[1]Some previous literature has defined "noncoherent squegging" (noise excited) and "coherent squegging" (remnant-energy excited) as two separate modes of behavior. From the viewpoint of the present analysis the distinction seems unnecessary since coherent squegging is actually no different from the remainder of the amplitude-modulated mode. In this report the term squegging oscillation will be used only in the case where each pulse grows from noise.

In the case of multimode operation, more than one mode of oscillation is possible for a given oscillator configuration. For example, two stable closed operating paths might exist in the (E, E_c)-plane. Or, as shown in Fig. 1.9, the point in the (E, E_c)-plane corresponding to a stable CW mode might be surrounded by an unstable closed operating path which in turn was surrounded by a stable closed operating path.

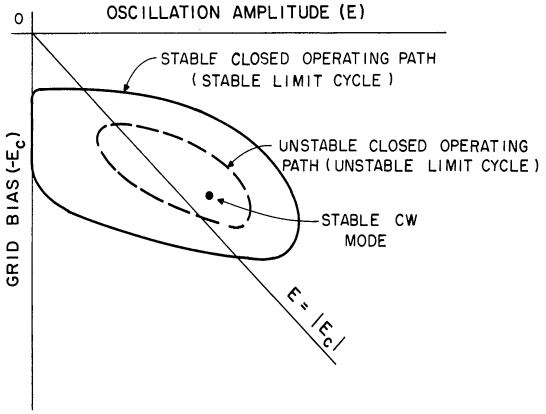

Fig. 1.9. Illustration of multimode operation.

Before proceeding it should be noted that a thorough appreciation of the details of the approximating procedure employed in Sections 2.2 and 2.3 is not a necessary prerequisite to an understanding of the remainder of this report. Therefore, a reader interested mainly in the final results and their application may find that simply skimming these two sections to pick out the details will suffice.

2. MATHEMATICAL CHARACTERIZATION

The mathematical characterization of the oscillator which is considered in this report (Fig. 1.1) is developed in this section. This characterization consists of a system of three first-order ordinary differential equations. Then another more tractable system of differential equations which is intended as an approximation to the original system is determined through careful inspection of this original system. The solution of this approximating system is carried out in Section 3 of

this report. The equations are first developed for specific grid-and plate-current characteristics, and then generalized so that they apply to arbitrary grid-and plate-current characteristics.

2.1 Equivalent Circuit

The circuit of the oscillator considered in this paper is shown in Fig. 1.1. An equivalent circuit for this oscillator is shown in Fig. 2.1. The plate circuit of the pentode has been replaced by an equivalent

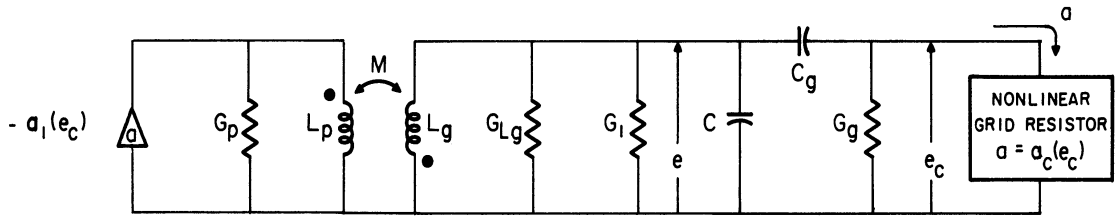

Fig. 2.1. Equivalent circuit for oscillator.

nonlinear grid-voltage-controlled current source whose characteristic is shown in Fig. 1.3. The grid conduction of the pentode has been modeled by a nonlinear resistor whose characteristic is shown in Fig. 1.2. The various symbols in Fig. 2.1 designate the following circuit elements.

$a_1(e_c)$ = pentode plate current as a function of pentode grid voltage. It is assumed that a_1 is independent of the pentode plate voltage. A plot of a specific $a_1(e_c)$ is shown in Fig. 1.3. (The symbol "a" has been used to denote current quantities throughout this report in order to avoid the confusing "$\dot{i}$" representation for di/dt.)

G_p = the equivalent shunt conductance combining losses in L_p and the pentode plate resistance.

L_p = the inductance of the plate coil. It is assumed that the distributed capacitance of this inductance may

be neglected.

L_g = the inductance of the grid coil.

M = the mutual inductance between L_p and L_g. M is always positive for the cases of interest.

G_{L_g} = the equivalent shunt conductance due to losses in L_g.

G_l = the conductance associated with an external load.

C = tank circuit capacitance. This capacitance includes the distributed capacitance of L_g.

C_g = the grid leak capacitance.

G_g = the grid leak conductance.

$a_c(e_c)$ = pentode current as a function of the grid voltage. A plot of a specific $a_c(e_c)$ is shown in Fig. 1.2.

Assuming that

$$Q_p = \frac{1}{\omega L_p G_p} > 10 ,$$

it is easily shown that the equivalent circuit in Fig. 2.1 can be replaced by the even simpler equivalent circuit in Fig. 2.2. The new elements which appear in Fig. 2.2 have the following definitions:

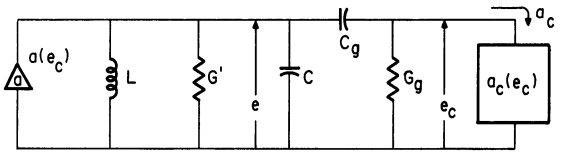

Fig. 2.2. Simplified equivalent circuit for oscillator.

$$a = \frac{M}{L_g} a_1 ,$$

$$L = L_g ,$$

$$G' = G_l + G_{L_g} + \frac{M^2}{L_g^2} G_p .$$

The circuit shown in Fig. 2.2 is the center of attention throughout the remainder of this report.

2.2 Mathematical Characterization of the Oscillator

The mathematical characterization of the simplified equivalent circuit shown in Fig. 2.2 is readily shown to be

$$\begin{cases} G'e + \frac{1}{L}\int e dt + C\frac{de}{dt} + C_g\frac{d}{dt}(e - e_c) - a(e_c) = 0 & (2.1) \\ G_g e_c + a_c(e_c) + C_g\frac{d}{dt}(e_c - e) = 0 . & (2.2) \end{cases}$$

Differentiating Eq. 2.1 and letting $\dot{e} = de/dt$, $\ddot{e} = d^2e/dt^2$, etc, gives

$$\begin{cases} \ddot{e} + \frac{G'}{C}\dot{e} + \frac{1}{LC}e + \frac{C_g}{C}(\ddot{e} - \ddot{e}_c) - \frac{\dot{a}(e_c)}{C} = 0 & (2.3) \\ G_g e_c + a_c(e_c) - C_g(\dot{e} - \dot{e}_c) = 0 . & (2.4) \end{cases}$$

Differentiating Eq. 2.4 and substituting into Eq. 2.3 gives

$$\begin{cases} \ddot{e} + \frac{G'}{C}\dot{e} + \frac{1}{LC}e + \frac{1}{C}\left[G_g\dot{e}_c + \frac{da_c}{de_c}\dot{e}_c - \frac{da}{de_c}\dot{e}_c\right] = 0 & (2.5) \\ (\dot{e}_c - \dot{e}) + \frac{G_g}{C_g}e_c + \frac{a_c(e_c)}{C_g} = 0 . & (2.2) \end{cases}$$

The system formed by Eqs. 2.2 and 2.5 can be transformed into a system of three first-order equations by introducing the new variable b, where

$$b = \dot{e} . \qquad (2.6)$$

The resulting system is

$$\begin{cases} \dot{e} = b, & (2.7) \\ \dot{e}_c = b - \frac{G_g}{C_g}e_c - \frac{a_c(e_c)}{C_g}, & (2.8) \\ \dot{b} = -\frac{1}{C}\left(G' + G_g + \frac{da_c}{de_c} - \frac{da}{de_c}\right)b - \frac{1}{LC}e \\ \qquad + \frac{1}{CC_g}\left[G_g e_c + a_c(e_c)\right]\left[\frac{da_c}{de_c} - \frac{da}{de_c} + G_g\right], & (2.9) \end{cases}$$

which is in the customary form for a system of three first-order

differential equations; that is,

$$\begin{cases} \dot{e} = g_1(e, e_c, b) , \\ \dot{e}_c = g_2(e, e_c, b) , \\ \dot{b} = g_3(e, e_c, b) . \end{cases} \tag{2.10}$$

Equations 2.7, 2.8, and 2.9 comprise the desired mathematical characterization of the equivalent circuit shown in Fig. 2.2.

2.3 Determination of the Approximating System of Differential Equations

An approximating system of differential equations is selected in this section. In order to make this selection more plausible, a coordinate transformation is used to recast the system represented by Eqs. 2.7, 2.8, and 2.9 into a form which allows physical intuition to be employed in the selection of the approximating system.

The coordinate transformation in question is of the following form:

$$\begin{cases} e = E \cos \psi , & (2.11) \\ e_c = E_c + E \cos \psi , & (2.12) \\ b = -\omega_o E \sin \psi , & (2.13) \end{cases}$$

where $\omega_o = 1/\sqrt{LC}$ is a constant, and in certain manipulations which follow the substitution $\psi = \omega_o t + \theta$ is employed. Since the Jacobian of this transformation is given by

$$\frac{\partial(e, e_c, b)}{\partial(E, E_c, \psi)} = \det \begin{vmatrix} \cos \psi & 0 & -E \sin \psi \\ \cos \psi & 1 & -E \sin \psi \\ -\omega_o \sin \psi & 0 & -\omega_o E \cos \psi \end{vmatrix} = -E\omega_o , \tag{2.14}$$

it follows that Eqs. 2.11, 2.12, and 2.13 form a satisfactory coordinate transformation when $E \neq 0$.

Application of the foregoing coordinate transformation to the system represented by Eqs. 2.7, 2.8, and 2.9 results in a new system of the following form.

$$\begin{cases} \dot{E} = h_1(E, E_c, \psi) , \\ \dot{E}_c = h_2(E, E_c, \psi) , \\ \dot{\psi} = h_3(E, E_c, \psi) , \end{cases} \tag{2.15}$$

where h_1, h_2, h_3 are periodic in ψ with period 2π.

It should be realized that the above system is still exactly equivalent to the original system given by Eqs. 2.1 and 2.2. As yet no approximations have been made; only coordinate transformations and substitutions have been employed. Clearly, it is only necessary to find the solutions of the above system, Eq. 2.15, in order to determine completely and exactly the behavior of the simplified equivalent circuit shown in Fig. 2.2. Unfortunately, this task is not easy. Therefore, another, more tractable system is considered instead of Eq. 2.15. This approximating system of equations must satisfy two important requirements; (1) it must be possible to integrate the system by simple methods (in this case graphical), and (2) its solutions must well approximate those of Eq. 2.15. Proving that the second of these two requirements has indeed been satisfied is by no means a trivial problem and is not attempted in this report. However, it is shown that the solutions obtained through consideration of the approximate system do agree well with experimentally observed solutions. Moreover, a certain amount of intuitive justification is employed in the selection of the approximating system.

At this point the line of reasoning which is followed is the same as the line of reasoning employed by Kryloff and Bogoliuboff [Ref. 2].

Integration of Eq. 2.15 over an interval of length T and division by T, where T is a nonzero constant, gives

$$\begin{aligned}
\frac{E(t+T) - E(t)}{T} &= \frac{1}{T}\int_t^{t+T} h_1[E(\xi), E_c(\xi), \psi(\xi)]d\xi \\
\frac{E_c(t+T) - E_c(t)}{T} &= \frac{1}{T}\int_t^{t+T} h_2[E(\xi), E_c(\xi), \psi(\xi)]d\xi \qquad (2.16) \\
\frac{\psi(t+T) - \psi(t)}{T} &= \frac{1}{T}\int_t^{t+T} h_3[E(\xi), E_c(\xi), \psi(\xi)]d\xi \ ,
\end{aligned}$$

Now assume that for sufficiently small T, $e_c(t)$ [$e_c(t) = E_c(t) + E(t)\cos\psi(t)$] is "locally cosinusoidal"; that is, $e_c(t)$ can be well approximated within the interval of integration of Eq. 2.16 by $E_c + E\cos(\omega t + \theta_o)$, where E_c, E, ω, and θ_o are constants. Note that among other things this assumption implies that the "RF" components on either side of the capacitance, C_g, in Fig. 2.2 are equal to one another (see Eqs. 2.11, 2.12, and 2.13). This consequence appears reasonable as long as

$$\frac{G_g + G_c}{\omega_o C} \ll 1 \ ,$$

where G_c is the slope in Fig. 1.2. The "locally cosinusoidal" behavior of $e_c(t)$ motivates the rewriting of Eq. 2.16 as follows:

$$\left\{\begin{aligned}
\frac{E(t+T) - E(t)}{T} &= \frac{1}{T}\int_t^{t+T} h_1(E, E_c, \lambda)d\xi + \frac{1}{T}\int_t^{t+T}\Big\{h_1[E(\xi), E_c(\xi), \psi(\xi)] \\
&\quad - h_1(E, E_c, \lambda)\Big\}\,d\xi \ , \\
\frac{E_c(t+T) - E_c(t)}{T} &= \frac{1}{T}\int_t^{t+T}\Big\{h_2(E, E_c, \lambda)d\xi + \frac{1}{T}\int_t^{t+T} h_2[E(\xi), E_c(\xi), \psi(\xi)] \\
&\quad - h_2(E, E_c\ \lambda)\Big\}\,d\xi \ , \qquad (2.16A) \\
\frac{\psi(t+T) - \psi(t)}{T} &= \frac{1}{T}\int_t^{t+T}\Big\{h_3(E, E_c, \lambda)d\xi + \frac{1}{T}\int_t^{t+T} h_3[E(\xi), E_c(\xi), \psi(\xi)] \\
&\quad - h_3(E, E_c, \lambda)\Big\}\,d\xi \ ,
\end{aligned}\right.$$

where $\lambda = \omega\xi + \theta_o$. It is then assumed that in each of the above equations the approximation is sufficiently close to $e_c(t)$ to allow the second integral to be ignored relative to the first integral. If T is then set equal to $2\pi/\omega$ and it is noted that each $h_j(E, E_c, \lambda)$ $(j = 1, 2, 3)$ is periodic in λ with period 2π, or ξ with period $2\pi/\omega$, the right-hand sides of Eq. 2.16-A can be approximated as follows:

$$\begin{cases} \dfrac{\Delta E}{\Delta t} = \dfrac{1}{2\pi}\displaystyle\int_o^{2\pi} h_1(E, E_c, \lambda)d\lambda = f_1(E, E_c) , \\ \dfrac{\Delta E_c}{\Delta t} = \dfrac{1}{2\pi}\displaystyle\int_o^{2\pi} h_2(E, E_c, \lambda)d\lambda = f_2(E, E_c) , \\ \dfrac{\Delta \psi}{\Delta t} = \dfrac{1}{2\pi}\displaystyle\int_o^{2\pi} h_3(E, E_c, \lambda)d\lambda = f_3(E, E_c) , \end{cases} \tag{2.17}$$

where $\Delta t = T$, $\Delta E = E(t - T) - E(t)$, $\Delta E_c = E_c(t + T) - E_c(t)$, and $\Delta\psi = \psi(t + T) - \psi(t)$. The final step in the selection of an approximate system of differential equations is simply to replace Eq. 2.17 by the system of differential equations which it suggests. Thus, the approximate system is selected as follows:

$$\begin{cases} \dfrac{dE}{dt} = f_1(E, E_c) , \\ \dfrac{dE_c}{dt} = f_2(E, E_c) , \\ \dfrac{d\psi}{dt} = f_3(E, E_c) . \end{cases} \tag{2.18}$$

This system of equations is the approximate system which replaces the exact system given by Eq. 2.15. It must be emphasized once more that the above system is considered <u>instead</u> of the exact system. The arguments which lead up to Eqs. 2.18 are <u>not</u> a rigorous justification for their use.

but only a demonstration that this substitution of Eq. 2.18 for Eq. 2.15 is at least plausible. Finally, it might be noted that at no point in the above discussion has it been necessary to determine explicitly the period, T, or its counterpart the frequency ω.

It now remains to determine the form of the functions $f_1(E, E_c)$, $f_2(E, E_c)$, and $f_3(E, E_c)$. The first step in this determination is the use of the coordinate transformation given in Eqs. 2.11, 2.12, and 2.13 to transform the dependent variables in the system of differential equations given by Eqs. 2.7, 2.8, and 2.9. This latter system is re-written below.

$$\begin{cases} \dot{e} = b \\ \dot{e}_c = b - \alpha(e_c) \\ \dot{b} = -\beta(e_c)b - \omega_o^2 e + \gamma(e_c) , \end{cases} \tag{2.19}$$

The following substitutions have been made;

$$\omega_o^2 = \frac{1}{LC} , \tag{2.19a}$$

$$G = G' + G_g , \tag{2.19b}$$

$$\alpha(e_c) = \frac{1}{C_g}\left[G_g e_c + a_c(e_c)\right] , \tag{2.19c}$$

$$\beta(e_c) = \frac{1}{C}\left\{G + g_c(e_c) - g_m(e_c)\right\} , \tag{2.19d}$$

$$\gamma(e_c) = \frac{1}{CC_g}\left\{\left[G_g e_c + a_c(e_c)\right]\left[G_g + g_c(e_c) - g_m(e_c)\right]\right\} \tag{2.19e}$$

where:

$$g_c(e_c) = \frac{da_c}{de_c} \tag{2.19f}$$

and

$$g_m(e_c) = \frac{da}{de_c} . \tag{2.19g}$$

Carrying out the coordinate transformation of the dependent variables presented in Eq. 2.14 gives the following system of equations.

$$\begin{cases} \dot{E} = -\beta(E, E_c, \psi)\, E \sin^2\psi - \dfrac{\gamma(E, E_c, \psi)}{\omega_o} \sin\psi\,, \\ \dot{E}_c = -\alpha(E, E_c, \psi) \\ \dot{\psi} = \omega_o - \beta(E, E_c, \psi) \sin\psi \cos\psi - \dfrac{\gamma(E, E_c, \psi)}{E\omega_o} \cos\psi \end{cases} \tag{2.20}$$

The above system corresponds to Eq. 2.15.

The system of equations corresponding to Eq. 2.18 is given by

$$\begin{aligned} \dot{E} &= \frac{1}{2\pi} \int_o^{2\pi} \left[-\beta(E, E_c, \lambda) E \sin^2\lambda - \frac{\gamma(E, E_c, \lambda)}{\omega_o} \sin\lambda \right] d\lambda \\ \dot{E}_c &= \frac{1}{2\pi} \int_o^{2\pi} \left[-\alpha(E, E_c, \lambda) \right] d\lambda \\ \dot{\psi} &= \frac{1}{2\pi} \int_o^{2\pi} \left[\omega_o - \beta(E, E_c, \lambda) \sin\lambda \cos\lambda - \frac{\gamma(E, E_c, \lambda)}{E\omega_o} \cos\lambda \right] d\lambda. \end{aligned} \tag{2.21}$$

Before the integrals (2.21) can be evaluated, it is necessary to determine the exact expressions for $\alpha(E, E_c, \psi)$, $\beta(E, E_c, \psi)$, and $\gamma(E, E_c, \psi)$. Referring to the definitions of these functions which follow Eq. 2.19, it can be seen that the determination of α, β, and γ reduces to the determination of $g_c(e_c) = da_c/de_c$, $g_m(e_c) = da/de_c$, and $a_c(e_c)$. A wide choice is possible for these functions, but (as mentioned previously) a specific set of functions will be employed here in order to go through the analysis, which follows in some detail. The assumed dependence of a_c on e_c

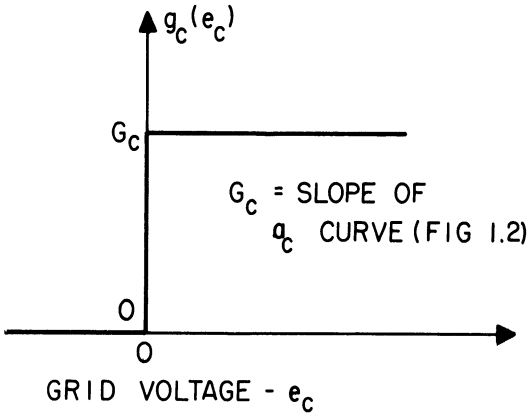

Fig. 2.3. Grid conductance versus e_c.

is shown in Fig. 1.2. Figure 1.2 also indicates the dependence of g_c upon e_c which is depicted in Fig. 2.3. Similarly, it follows from Fig. 1.3 and the definition of $a(e_c)$[1] that the dependence of g_m upon e_c is as shown in Fig. 2.4. Substituting for e_c by means of Eq. 2.12 gives g_m, g_c, and a_c as functions of E, E_c, and λ (recall that $\psi \rightarrow \lambda$); that is,

$$g_c(E, E_c, \lambda) = g_c(E_c + E \cos \lambda)$$

$$g_m(E, E_c, \lambda) = g_m(E_c + E \cos \lambda)$$

and

$$a_c(E, E_c, \lambda) = a_c(E_c + E \cos \lambda) .$$

For the integration of Eq. 2.21, the dependence of g_m, g_c, and a_c upon λ must be known. E and E_c are treated as parameters insofar as these integrals are concerned. A typical situation is illustrated in Fig. 2.5. In this figure note that the symbol σ has been introduced for the conduction angle. Thus,

$$\sigma = \begin{cases} \cos^{-1}\left(\dfrac{R - E_c}{E}\right) & \text{for } E \geq |R - E_c| \\ 0 & \text{for } E_c \leq R \text{ and } E < |R - E_c| \\ \pi & \text{for } E_c \geq R \text{ and } E < |R - E_c| . \end{cases} \quad (2.22)$$

This symbol, σ, simplifies certain equations that appear later in this report. The dependence of g_c and a_c upon λ is similar to the dependence of g_m upon λ as depicted in Fig. 2.5. In the case of g_c and a_c the conduction angle is designated φ and defined as follows:

$$\varphi = \begin{cases} \cos^{-1}\left(-\dfrac{E_c}{E}\right) & \text{for } E \geq |E_c| , \\ 0 & \text{for } E < |E_c| . \end{cases} \quad (2.23)$$

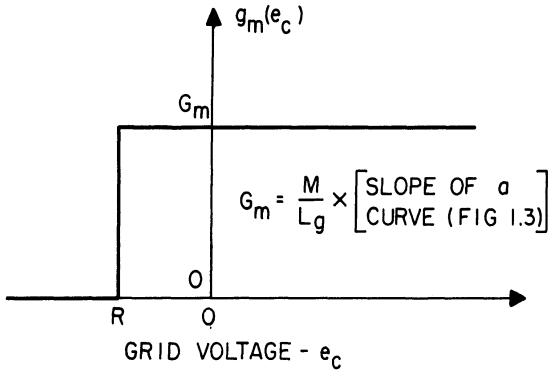

Fig. 2.4. Plate transconductance versus e_c.

[1] See p. 13.

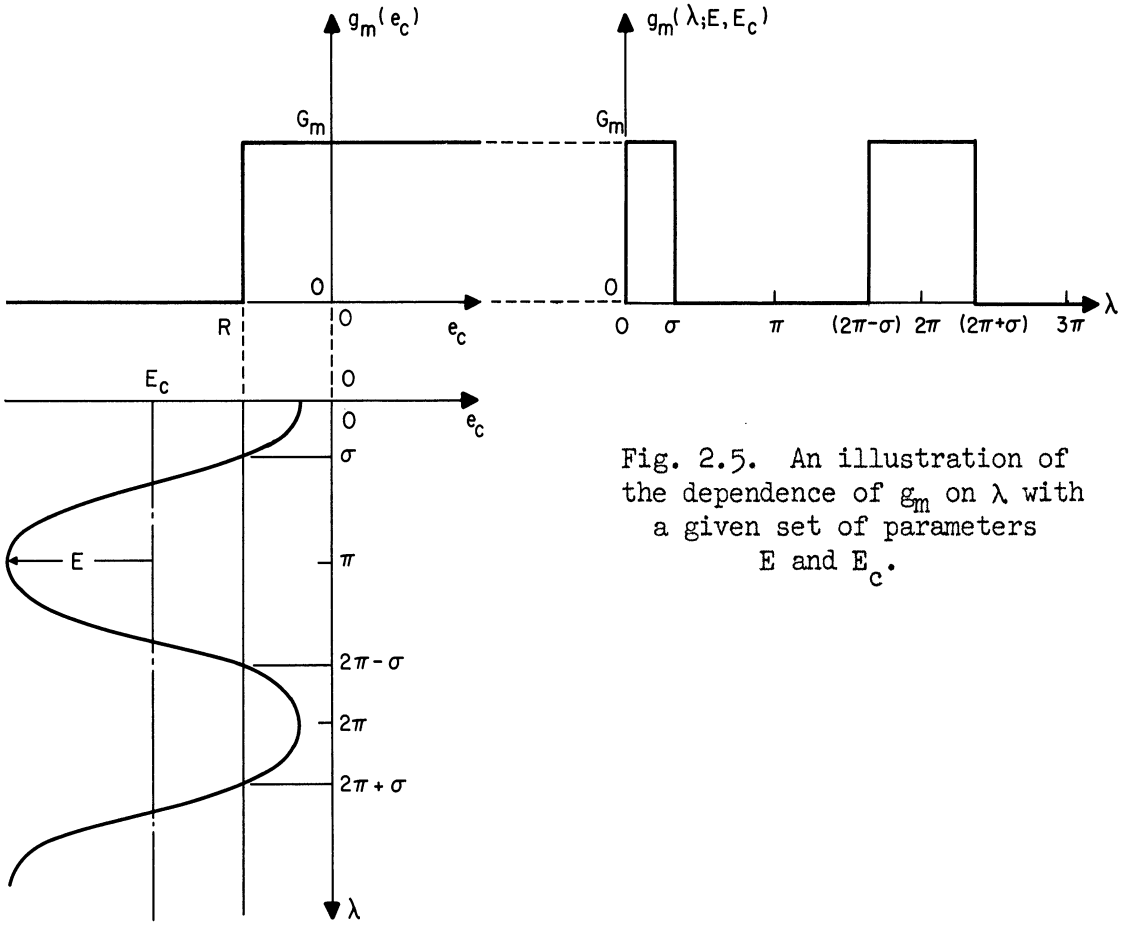

Fig. 2.5. An illustration of the dependence of g_m on λ with a given set of parameters E and E_c.

It then follows from Figs. 1.2 and 2.5 and Eqs. 2.22 and 2.23 that

$$g_c(E_c + E\cos\lambda) = \begin{cases} G_c \text{ for } 0 \le \lambda \le \varphi \text{ and } (2\pi - \varphi) \le \lambda \le 2\pi \,, \\ \\ 0 \text{ for } \varphi < \lambda < (2\pi - \varphi) \,, \end{cases} \tag{2.24}$$

$$g_m(E_c + E\cos\lambda) = \begin{cases} G_m \text{ for } 0 \le \lambda \le \sigma \text{ and } (2\pi - \sigma) \le \lambda \le 2\pi \,, \\ \\ 0 \text{ for } \sigma < \lambda < (2\pi - \sigma) \,, \end{cases} \tag{2.25}$$

and

$$a_c(E_c + E\cos\lambda) = \begin{cases} G_c(E_c + E\cos\lambda) \text{ for} \\ \qquad 0 \le \lambda \le \varphi \text{ and } (2\pi - \varphi) \le \lambda \le 2\pi \\ \\ 0 \text{ for } \varphi < \lambda < (2\pi - \varphi) \end{cases} \tag{2.26}$$

Substituting Eqs. 2.24, 2.25, and 2.26 into Eq. 2.22 and carrying out the indicated integrations gives the following system of equations.

$$\begin{cases} \dot{E} = \dfrac{E}{2C}\left[\dfrac{G_m}{\pi}\left(\sigma - \dfrac{1}{2}\sin 2\sigma\right) - \dfrac{G_c}{\pi}\left(\varphi - \dfrac{1}{2}\sin 2\varphi\right) - G\right] \\ \dot{E}_c = -\dfrac{E_c}{C_g}\left[G_g + \dfrac{G_c}{\pi}\left(\varphi + \dfrac{E}{E_c}\sin\varphi\right)\right], \\ \dot{\psi} = \omega_o - \dfrac{1}{2CC_g\omega_o}\left\{G_c^2 - \dfrac{G_c}{\pi}(G_c + 2G_g - G_m)\left(\varphi + \dfrac{1}{2}\sin 2\varphi\right) + \dfrac{G_g G_m}{\pi}\right. \\ \qquad \left.(\sigma + \dfrac{1}{2}\sin 2\sigma) - \dfrac{E_c}{E}\left[\dfrac{2G_c}{\pi}(G_c + 2G_g - G_m)\sin\varphi + \dfrac{2G_m G_g}{\pi}\sin\sigma\right]\right\} \end{cases} \tag{2.27}$$

The above system constitutes the approximating system of differential equations and is equivalent to Eq. 2.18. The analysis of this system is carried out in the following section of this report. However, before going on to this analysis it is worthwhile to recapitulate the assumptions which are associated with the selection of Eq. 2.27. These assumptions are as follows:

(a) $Q_p \geq 10$ and capacity on plate side of transformer is negligible. (Introduced just preceding Fig. 2.2.)

(b) $E(t)$, $E_c(t)$, and $[\psi(t) - \omega t]$, the variables associated with the original system, Eq. 2.20, are slowly varying functions of time relative to a "period of oscillation" T; i.e.,

$\left|\dfrac{\dot{E}T}{E}\right|$, $\left|\dfrac{\dot{E}_c T}{E_c}\right|$, and $\left|\left(\dfrac{\dot{\psi} - \omega}{\omega}\right)T\right|$ are small quantities. (See the discussion following Eq. 2.16.)

(c) $\dfrac{G_g + G_c}{\omega_o C_g} \ll 1$ (See the discussion following Eq. 2.16)

3. Solution of the Approximating System of Differential Equations

The approximating system of differential equations, Eq. 2.27, was developed in the foregoing section. In this section, a phase plane is introduced which is suitable for determining the solutions of this approximating system. A detailed discussion of the implications of this phase plane is then carried out in Section 4 of this report.

Referring to Eq. 2.27, it can be seen that the approximating system is a second-order system, although at first glance it might appear to be a third-order system. This fact can be appreciated by noting that all three derivatives, $\dot{E}$, $\dot{E}_c$, and $\dot{\psi}$ are functions of E and E_c only: ψ does not appear on the right-hand side of any of these three equations. Consequently, the first two equations form a system which is independent of the third equation. ψ itself can be determined from a straightforward integration of the third equation. However, the resulting $\psi(t)$ is not a satisfactory approximation to the $\psi(t)$ which is associated with the original differential equation, Eq. 2.19. This merely means that the approximating system which has been selected here does not yield useful information about the variations in the instantaneous frequency of oscillation. Since a method which is essentially similar to the one employed in this report does not result in satisfactory information about frequency shifts for even a linear system [Ref. 3], the limitations of the present method are not surprising.

The mathematical characterization of the E and E_c variations is, therefore, of the form

$$\begin{cases} \dot{E} = \dfrac{-E}{2C}\left[G - \dfrac{G_m}{\pi}\left(\sigma - \dfrac{1}{2}\sin 2\sigma\right) + \dfrac{G_c}{\pi}\left(\varphi - \dfrac{1}{2}\sin 2\varphi\right)\right], \\ \dot{E}_c = \dfrac{-E_c}{C_g}\left[G_g + \dfrac{G_c}{\pi}\left(\varphi + \dfrac{E}{E_c}\sin\varphi\right)\right]. \end{cases} \tag{3.1}$$

Formally, the general solution of the above system is

$$\begin{cases} E = E\left\{(t - t_o);\ E_o,\ E_{co}\right\}, \\ E_c = E_c\left\{(t - t_o);\ E_o,\ E_{co}\right\}, \end{cases} \tag{3.2}$$

where E_o and E_{co} are the values of E and E_c, respectively, at $t = t_o$. Thus, given initial conditions E_o and E_{co} and an initial time, t_o (usually t_o can be assumed equal to zero), a solution of Eq. 3.1 is formally represented by Eq. 3.2. A solution of special interest would be one for which the right-hand sides of Eq. 3.1 vanish simultaneously Such a solution would correspond to a CW mode of oscillation and be of the form

$$\begin{aligned} E &= \text{a constant}, \\ E_c &= \text{a constant}. \end{aligned} \tag{3.3}$$

It is clear from the form of Eq. 3.1 that standard phase plane techniques [Ref. 4] can now be employed to investigate its solutions. However, before a phase plane is introduced it is worthwhile first to consider carefully the form of Eq. 3.1. In particular, note that the terms inside of the brackets in Eq. 3.1 can be identified as conductances or averaged conductances. In the first equation, G is the conductance associated with the tank circuit losses; that is, G is a linear conductance. In the same equation, the expression

$$\frac{G_c}{\pi}\left(\varphi - \frac{1}{2}\sin 2\varphi\right)$$

can be considered to be a voltage-dependent conductance which is associated with the high frequency current flow in the grid. The voltage dependence is clear from the definition of φ, Eq. 2.23. Let

$$G_c^{hf}\left\{E,\ E_c\right\} \equiv \frac{G_c}{\pi}\left(\varphi - \frac{1}{2}\sin 2\varphi\right) \tag{3.4}$$

It can be shown that for grid current versus grid voltage and associated $g_c(e_c)$ characteristics other than the ones presented in Figs. 1.2 and 2.3

$$G_c^{hf}\{E, E_c\} \equiv \frac{1}{\pi}\int_0^{2\pi} g_c(E_c + E\cos\psi)\sin^2\psi \; d\psi \; . \qquad (3.5)$$

The remaining expression inside the brackets of the first equation of Eq. 3.1 is

$$\frac{G_m}{\pi}(\sigma - \frac{1}{2}\sin 2\sigma) \; .$$

In a manner which is similar to the definition of G_c^{hf}, this remaining term can be considered to be a voltage-dependent conductance arising from tube amplification. Thus, let

$$G_m^{hf}\{E, E_c\} \equiv \frac{G_m}{\pi}(\sigma - \frac{1}{2}\sin 2\sigma) \; , \qquad (3.6)$$

and in the general case with plate current versus grid voltage and associated $g_m(e_c)$ characteristics other than the ones presented in Figs. 1.3 and 2.4,

$$G_m^{hf}\{E, E_c\} \equiv \frac{1}{\pi}\int_0^{2\pi} g_m(E_c + E\cos\psi)\sin^2\psi \; d\psi \; . \qquad (3.7)$$

Note that G_m^{hf} is the "average g_m" which was mentioned in Section 1.

In the second equation of Eq. 3.1 there are two terms inside the brackets. The first term, G_g, is just the linear conductance of the grid leak bias circuit. The second term is

$$\frac{G_c}{\pi}(\varphi + \frac{E}{E_c}\sin\varphi) \; .$$

This term can be considered to be a voltage-dependent conductance associated with low frequency current flow in the grid. Let

$$G_c^{lf} \equiv \frac{G_c}{\pi}(\varphi + \frac{E}{E_c}\sin\varphi) \; . \qquad (3.8)$$

In the general case with a grid-current versus grid-voltage characteristic other than the one shown in Fig. 1.2,

$$G_c^{1f} = \frac{1}{2\pi E_c} \int_0^{2\pi} a_c\{E_c + E \cos \psi\} d\psi \ . \tag{3.9}$$

Substituting Eqs. 3.4, 3.6, and 3.8 into Eq. 3.1 results in the following simplified expression:

$$\begin{aligned} \dot{E} &= \frac{-E}{2C}\left[G - G_m^{hf}\{E, E_c\} + G_c^{hf}\{E, E_c\}\right] \\ \dot{E}_c &= \frac{-E_c}{C_g}\left[G_g + G_c^{1f}\{E, E_c\}\right] . \end{aligned} \tag{3.10}$$

This expression together with Eqs. 3.5, 3.7, and 3.9 is the generalized approximate system of equations which applies to oscillators which have grid and plate characterizations other than those shown in Figs. 1.2 and 1.3.

The construction of an (E, E_c)-phase plane for the specific oscillator characterized by Eqs. 3.10, 3.4, 3.6, and 3.8 can be carried out in a straightforward manner. In order to determine the direction of the solution path through any point (x, y) in the phase plane it is merely necessary to substitute the appropriate values $E = x$ and $E_c = y$ into the right-hand side of Eq. 3.10 and then use the resulting $\dot{E}$ and $\dot{E}_c$ to determine the solution path direction as demonstrated in Fig. 3.1.

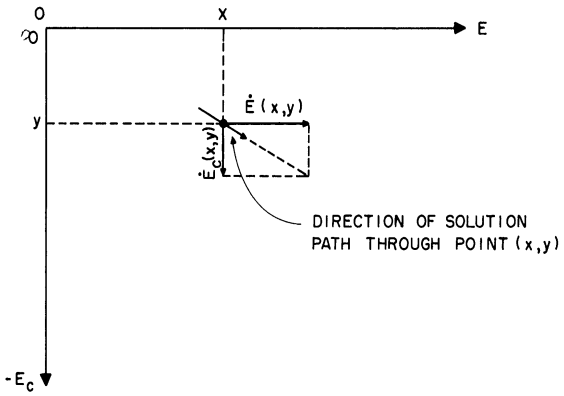

Fig. 3.1. Illustration of method of constructing of solution paths in the (E, E_c)-phase plane.

Owing to the relative complexity of the right-hand side of Eq. 3.10, it is not particularly helpful to employ the method of iso-

clines, which is often used in the construction of phase planes. However, the two equations of Eq. 3.10 can be used separately to determine $\dot{E}$ or $\dot{E}_c$ versus E and E_c surfaces, and these surfaces are an aid in either the construction of the phase plane or a visualization of its construction. Using the $a_c(e_c)$ and $a(e_c)$ characteristics of Figs. 1.2 and 1.3, these surfaces appear as shown in Figs. 3.2 and 3.3.

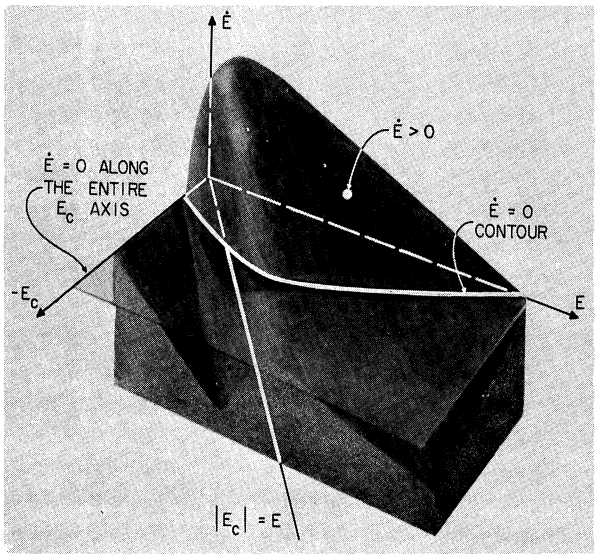

Fig. 3.2. Typical $\dot{E}$ versus (E, E_c) surface.

It follows from the surfaces of Figs. 3.2 and 3.3 that the phase-plane configuration for Eq. 3.1 is similar to the typical one shown in Fig. 3.4. Needless to say, the appropriate phase plane for a particular set of oscillator parameters, although to some extent similar to Fig. 3.4, can be significantly different in character.

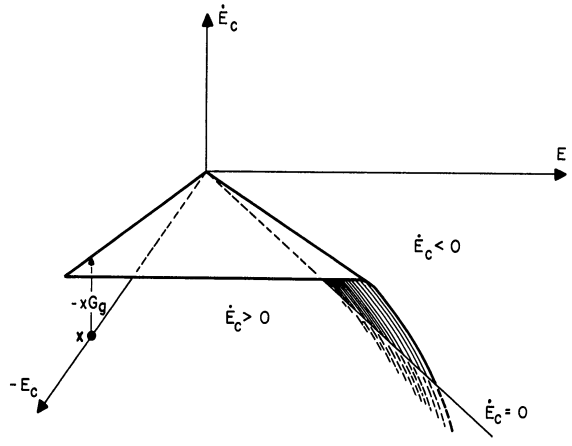

Fig. 3.3. Typical $\dot{E}_c$ versus (E, E_c) surface.

The particular example given in Fig. 3.4 shows the phase-plane configuration for an oscillator which exhibits only a stable CW mode of oscillation. As is discussed in detail in Section 4, other modes of oscillation are possible and have their corresponding phase-plane configurations.

Before going on to Section 4 it is worthwhile to consider just a few of the salient features of Fig. 3.4. First, note that the contours of $\dot{E} = 0$ and $\dot{E}_c = 0$ from Figs. 3.2 and 3.3 are shown in Fig. 3.4 (notice that the $\dot{E} = 0$ contour also includes the E_c-axis). The intersections of these two contours obviously correspond to two equilibrium points, where one is stable and the other is unstable. The dashed curve shown in Fig. 3.4 is the $E = |E_c|$ locus. Its significance is that it divides those combinations of E and E_c for which grid current flows from those combinations for which no grid current flows. These curves maintain roughly the same topological relation to one another as circuit parameters are varied, even though the $\dot{E} = 0$ and $\dot{E}_c = 0$ contours do shift in the phase plane. Consequently, these curves are used extensively in the discussions in Section 4.

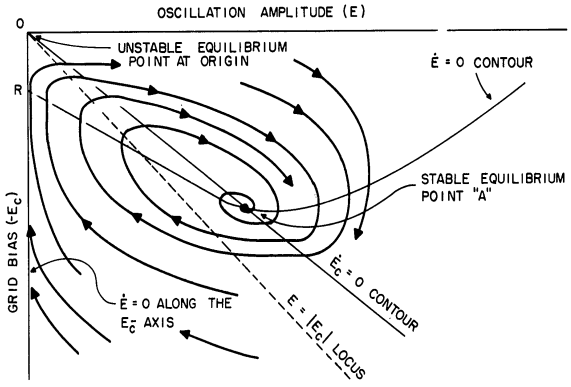

Fig. 3.4. Typical phase-plane representation of the approximating system.

4. PHASE-PLANE CONFIGURATIONS AND MODES OF OSCILLATION PREDICTED BY THE MATHEMATICAL ANALYSIS

4.1 Introduction

In the foregoing sections, a mathematical model for the oscillator circuit of interest was developed and a phase plane in which solutions for this mathematical model could be determined was introduced. It was also shown that generalized conductances (see Eqs. 3.5, 3.7, and 3.9) could be defined and employed when grid and plate characteristics other than those shown in Figs. 1.2 and 1.3 were of interest. The various

phase-plane configurations which are of interest and their associated modes of oscillation are discussed in this section. Most of the remarks in this section apply to the case in which generalized conductances are considered, although the examples presented are limited to the originally assumed grid and plate characteristics.

The phase-plane configurations of interest are divided into three classes. The first class consists of all those phase-plane configurations in which there is only one stable equilibrium point and this equilibrium point is practically stable-in-the-large; that is, given almost any initial conditions the solution path converges to the stable equilibrium point[1]. This first class is discussed in Subsection 4.3 and is designated as the "Practically Stable-in-the-Large Equilibrium Point Phase-Plane Configuration" or the (PSLE) configuration.

The second class of phase-plane configurations consists of all those configurations in which there is at least one stable limit cycle and no stable equilibrium points. This second class is discussed in Subsection 4.4 and is designated "Stable-Limit-Cycle Unstable-Equilibrium-Point Phase-Plane Configuration" or the (SLC-UE) configuration.

The third class of phase-plane configurations consists of all those configurations in which there is at least one stable limit cycle and only one stable equilibrium point. This third class is discussed in Subsection 4.5 and is designated "Stable-Limit-Cycle Stable-Equilibrium-Point Phase-Plane Configuration" or the (SLC-SE) configuration.

---

[1] From a theoretical point of view it is not stable-in-the-large, because no initial conditions on the E_c-axis result in a solution which converges to the stable equilibrium point. Since $\dot{E} = 0$ but $\dot{E}_c > 0$ on the E_c axis, all solutions which start on the E_c axis converge to the unstable equilibrium point at the origin. Thus, this unstable equilibrium point must be a saddle point; therefore, for practical purposes, all solutions will bypass it and converge to the stable equilibrium point.

Associated with any given phase-plane configuration is one or more modes of oscillation. As was mentioned in the introduction of this report, these modes of oscillation are of three types. These types are (1) the CW mode, (2) the Amplitude-Modulated mode, and (3) the Squegging mode. Sometimes it is convenient to consider Amplitude-Modulated and Squegging modes together as a single mode. In that case the name "Limit-Cycle mode" is used. The relation between these modes of operation and the three classes of phase-plane configuration is brought out during the discussion of each configuration. In particular, it is shown that a given mode of oscillation is not necessarily associated with only one class of phase-plane configuration.

In the last subsection, the effect of varying a circuit parameter is discussed. The parameter considered as an example is the grid-leak conductance, G_g.

4.2 Determination of Waveforms from the Phase-Plane Configuration

Before going into a discussion of the various phase-plane configurations, a short review will be given of the method whereby the waveform associated with a given solution path in the phase plane can be determined. Consider the portion of a solution path shown in Fig. 4.1. It is assumed that this solution path results from an application of the technique illustrated in Fig. 3.1 to a pair of

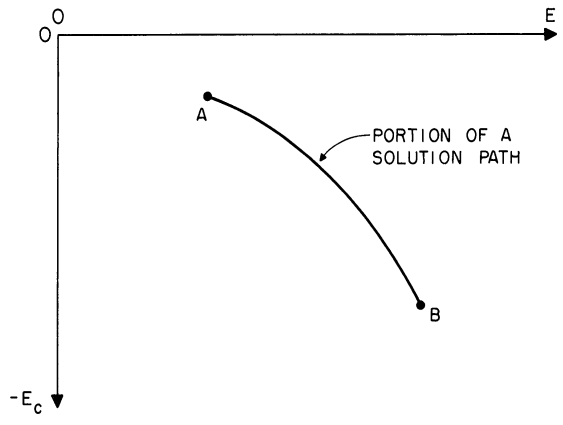

Fig. 4.1. Portion of a solution path in the phase-plane.

equations

$$\begin{cases} \dot{E} = f_1(E, E_c) \\ \dot{E}_c = f_2(E, E_c) \end{cases} .$$

It is not possible to determine E and E_c as functions of time from Fig. 4.1 alone. In order to make this determination, the value of $\dot{E}$ or $\dot{E}_c$ at each point along the solution path must be known. This information is available if the solution path shown in Fig. 4.1 is plotted onto the (E, E_c)-plane in either Fig. 3.2 or Fig. 3.3, or, similarly, if contours of the $\dot{E}$ or $\dot{E}_c$ surfaces are plotted onto Fig. 4.1. In either case curves of either $\dot{E}$ versus E or $\dot{E}_c$ versus E_c along the solution path can be determined. It then follows that the time interval between any two points (say points A and B in Fig. 4.1) can be determined by either of the following two line integrals:

$$\Delta t = \int_A^B \frac{1}{\dot{E}} \, dE ,$$

or

$$\Delta t = \int_A^B \frac{1}{\dot{E}_c} \, dE_c .$$

4.3 Practically Stable-in-the-Large Equilibrium Point Phase-Plane Configuration [The (PSLE) Configuration]

A (PSLE) configuration is, as the name implies, a phase-plane configuration in which there is only one stable equilibrium point and in which this equilibrium point is practically stable-in-the-large[1]. An example of a (PSLE) configuration is shown in Fig. 4.2. This figure presents the phase-plane configuration associated with the mathematical model when the specific grid and plate current characteristics of

[1]See the footnote on p. 30.

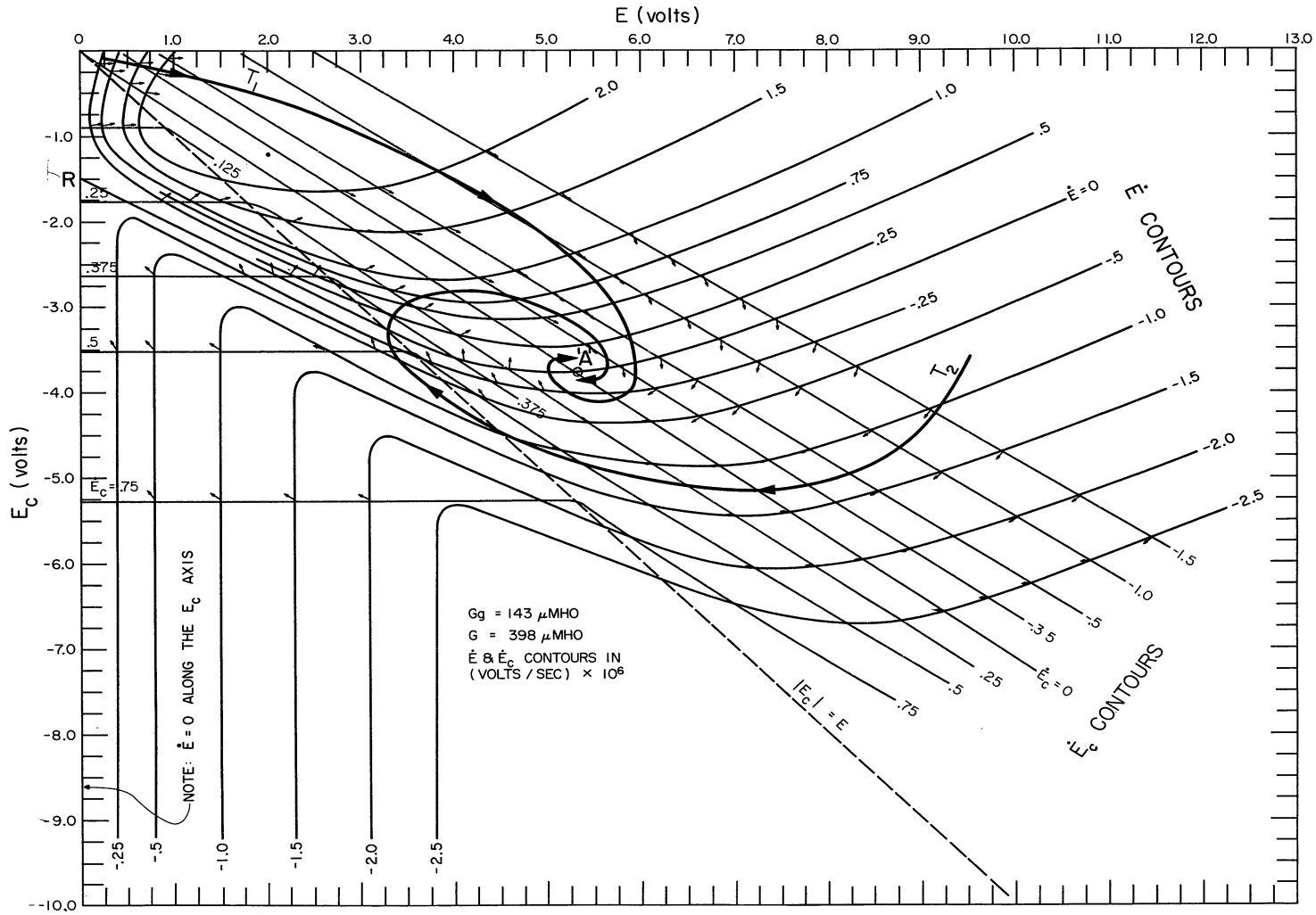

Fig. 4.2. (E, E_c)-plane diagram example of a (PSLE) configuration.

Figs. 1.2 and 1.3 are assumed. The model parameters used are[1]

$$G_m = 2390 \ \mu\text{mho}$$

$$G_c = 1920 \ \mu\text{mho}$$

$$G = G' + G_g = 398 \ \mu\text{mho}$$

$$C_g = 1000 \text{ pf}$$

$$C = 300 \text{ pf}.$$

In Fig. 4.2 the contours of both the $\dot{E}$ and $\dot{E}_c$ surfaces are shown and the direction of the solution paths at various points (found by the method illustrated in Fig. 3.1) are indicated by vectors. A significant feature of Fig. 4.2 is that with the exception of the E_c axis all initial conditions, E_o and E_{co}, result in solution paths which converge to the equilibrium point A. Two such solution paths are shown as T_1 and T_2 in the figure. Thus, if the coordinates of the Point A are designated E_A and E_{CA}, it is clear that after a transient interval[2] an oscillator characterized by the phase plane in Fig. 4.2 will reach a CW mode of oscillation which is of the form

$$\begin{aligned} e_c(t) &= E_{CA} + E_A \cos \omega_o t \\ e(t) &= E_A \cos \omega_o t \end{aligned} \qquad (4.1)$$

Moreover, this will be the only possible stable mode of oscillation. It is shown later that some of the other phase-plane configurations can have more than one stable mode of oscillation. If one were interested in designing a CW oscillator with grid-leak bias, it is evident that the (PSLE) configuration would be desirable.

---

[1] G' is defined on page 13. G_g is shown in Fig. 1.1.

[2] The waveform associated with the transient behavior may be determined by integration along the particular solution path as described in Section 4.2. For example, the waveform of oscillation built up from noise would be obtained from an integration along path T_1.

As has been mentioned previously, the approximating system of differential equations, (2.27), employed in this paper does not give a suitable approximation to the instantaneous frequency of oscillation. Consequently, the frequency of oscillation is arbitrarily assumed to be equal to ω_o in Eq. 4.1.

Ideally it would be desirable to be able to determine from the circuit parameter values whether or not the phase-plane configuration associated with a given oscillator is a (PSLE) configuration. Unfortunately, this determination is not easily completed. In particular, it is not easy to obtain necessary as well as sufficient conditions for a (PSLE) configuration. On the other hand, it is possible to determine in a straightforward manner whether the equilibrium point A is asymptotically stable-in-the-small, but the extension to stability-in-the-large is difficult. If a suitable Liapunov function were determined, Liapunov's Second Method could be used to obtain sufficient conditions but not necessary conditions. Consequently, only the conditions which are necessary and sufficient for the asymptotic stability-in-the-small of the equilibrium point A are presented in this subsection.

Asymptotic Stability-in-the-Small of the Equilibrium Point A:

The determination of necessary and sufficient conditions for the asymptotic stability-in-the-small of the equilibrium point A is accomplished with a standard linearization technique discussed in detail in many places [Refs. 3, 5]. Therefore, only the outline of the argument which leads up to the stability criterion is presented.

The system of differential equations under consideration is, again, of the form

$$\begin{cases} \dot{E} = f_1(E, E_c) , \\ \dot{E}_c = f_2(E, E_c) ; \end{cases} \tag{4.2}$$

and at the equilibrium point A, which has coordinates E_A and E_{CA}, the following conditions are satisfied by definition of an equilibrium point:

$$\begin{cases} f_1(E_A, E_{CA}) = 0 , \\ f_2(E_A, E_{CA}) = 0 . \end{cases} \tag{4.3}$$

Asymptotic stability-in-the-small is determined by the behavior of the solutions of Eq. 4.2 in the neighborhood of the equilibrium point A. Let

$$E = E_A + x$$

and

$$E_c = E_{CA} + y.$$

In a small neighborhood of the equilibrium point A, the linear approximation to Eq. 4.2 (i.e., the variational equation) is given by[1]

$$\begin{aligned} \dot{x} &= \left.\frac{\partial f_1}{\partial E}\right|_A x + \left.\frac{\partial f_1}{\partial E_c}\right|_A y , \\ \dot{y} &= \left.\frac{\partial f_2}{\partial E}\right|_A x + \left.\frac{\partial f_2}{\partial E_c}\right|_A y \end{aligned} \tag{4.4}$$

If the partial derivatives in Eq. 4.4 are denoted by[2]

---

[1] A is the point $E = E_A$, $E_c = E_{CA}$.

[2] When characteristics are as given in Figs. 1.2 and 1.3 and Eq. 3.1 applies, the partial derivatives are

$$f_{1E} = K_1 \sin 2\sigma_A - K_2 \sin 2\varphi_A = 2K_1\sigma_A - 2K_2\varphi_A - K_3 , \tag{4.4a}$$

$$f_{1E_c} = 2K_1 \sin \sigma_A - 2K_2 \sin \varphi_A , \tag{4.4b}$$

$$f_{2E} = -K_5 \sin \varphi_A , \tag{4.4c}$$

$$f_{2E_c} = -K_4 - K_5\varphi_A , \tag{4.4d}$$

where

$$K_1 = \frac{G_m}{2\pi c} \qquad K_2 = \frac{G_c}{2\pi c} \qquad K_3 = \frac{G}{2c}$$

$$K_4 = \frac{G_g}{G_g} \qquad K_5 = \frac{G_c}{\pi G_g}$$

and σ_A and φ_A are the conduction angles defined in Eqs. 2.22 and 2.23 and evaluated at the point A. It is seen later (Section 4.6) that equilibrium point A must occur in the region where

$$0 < \sigma < \pi$$

$$0 < \varphi < \frac{\pi}{2}$$

and thus at point A the Eqs. 2.22 and 2.23 describe a one-to-one relation between (E_A, E_{CA}) and (σ_A, φ_A).

In addition to stability tests the partial derivatives are frequently useful in investigating the behavior of the $\dot{E}$ and $\dot{E}_c$ surfaces throughout the plane. With the exception of f_{1E}, the above forms are valid at all points if the angles σ and φ are properly evaluated in accordance with their definitions (see Fig. 4.11). However f_{1E} was obtained by combining

$$\frac{\partial f_1}{\partial E} = K_1(\sigma + \tfrac{1}{2} \sin 2\sigma) - K_2(\varphi + \tfrac{1}{2} \sin 2\varphi) - K_3 ,$$

which is valid everywhere, with Eq. 4.12, which is valid only at point A. Thus, the original form, $\partial f_1/\partial E$, should be used at points other than point A.

$$\left.\frac{\partial f_j}{\partial E}\right|_A = f_{jE} \qquad (j = 1, 2) ,$$

and

$$\left.\frac{\partial f_j}{\partial E_c}\right|_A = f_{jE_c} \qquad (j = 1, 2) ,$$

it follows that the characteristic equation of the linear system (4.4), is given by

$$\lambda^2 - \left[f_{1E} + f_{2E_c}\right]\lambda + \left[f_{1E}f_{2E_c} - f_{1E_c}f_{2E}\right] = 0 . \qquad (4.5)$$

The equilibrium point A is asymptotically stable-in-the-small if both roots of Eq. 4.5 have negative real parts, and unstable if one or both roots have positive real parts. Whether or not both these real parts are negative could be determined by means of the quadratic formula. However, by using index theorems it is possible to develop a considerably simpler stability criterion.

First, note that if

$$f_{1E}f_{2E_c} - f_{1E_c}f_{2E} < 0 ,$$

the roots are both real and of opposite sign; therefore, the equilibrium point A is a saddle point, and if point A is a saddle point its index must be -1*. However, it is shown in Appendix A that under a few rather loose restrictions on the system the index of the equilibrium point A must be +1. Therefore, it follows that point A can not be a saddle point and

$$f_{1E}f_{2E_c} - f_{1E_c}f_{2E} > 0 .$$

The above inequality implies that the roots of Eq. 4.5 both have negative real parts if and only if

$$\boxed{f_{1E} + f_{2E_c} < 0 ,} \qquad (4.6)$$

*For a complete discussion of types of equilibrium points and indexes see [Ref. 5].

and both have positive real parts if and only if

$$\boxed{f_{1E} + f_{2E_c} > 0 \ .}$$

An application of the above criterion to Fig. 4.2 [either by measuring the slopes f_{1E} and f_{2E_c} in the figure or by using the relations (4.4a) and (4.4d) and the coordinates of the point A] shows that the equilibrium point is stable. Evaluation of the roots of the characteristic equation shows that the equilibrium point in Fig. 4.2 is a stable focus; thus, the spiraling of the vectors into point A is anticipated.

In addition to being a simple expression, the stability condition (4.6) allows certain conclusions to be drawn directly from the phase-plane configuration. This can be seen by referring to Fig. 4.2. Assume in this figure that the general shapes of the $\dot{E} = 0$ and the $\dot{E}_c = 0$ contours do not alter markedly as the circuit parameters are varied over small intervals. Then consider the sign of f_{1E} for various positions on the $\dot{E} = 0$ contour. Note that this contour takes on a minimum value of the ordinate, E_c, just to the left of point A. Since $\dot{E}$ is positive for all points above the $\dot{E} = 0$ contour and negative below, it follows by inspection that for all points on the $\dot{E} = 0$ contour to the left of the minimum E_c point

$$f_{1E} > 0.$$

Similarly, it follows that for all points to the right of this minimum E_c point

$$f_{1E} < 0 \ .$$

It also follows by inspection that for all points on the $\dot{E}_c = 0$ contour $f_{2E_c} < 0$. Consequently, the intersection of the $\dot{E} = 0$ and $\dot{E}_c = 0$ contours tells something about the stability characteristics. In particular, if the $\dot{E}_c = 0$ contour intersects the $\dot{E} = 0$ contour to the right of its minimum E_c point both f_{1E} and f_{2E_c} are negative; therefore, Eq. 4.6 is auto-

matically satisfied, and the equilibrium point A is stable. Furthermore, in order for the equilibrium point A to become unstable, the $\dot{E}_c = 0$ contour must intersect the $\dot{E} = 0$ contour sufficiently far to the left of its minimum E_c point to allow the positive f_{2E_c} to cancel out the negative f_{1E} in Eq. 4.6. In other words, the boundary point on the $\dot{E} = 0$ contour between stability and instability of the equilibrium point A is just to the left of the minimum E_c point.

4.4 Stable-Limit-Cycle Unstable-Equilibrium-Point Phase-Plane Configuration [The (SLC-UE) Configuration]

In this case the phase plane possesses two equilibrium points, point A and the origin, which are both unstable and at least one stable limit cycle encircling point A. All solution paths beginning at any point, except point A, inside this limit cycle converge to the limit cycle. This limit cycle may, in turn, be encircled by other limit cycles. The only requirements on the limit cycles is that the outermost be stable and that they alternate their stability characteristics; that is, the first is stable, the next is unstable, and so on. An example of an (SLC-UE) configuration is shown in Fig. 4.3. This figure presents the phase-plane configuration which is associated with the mathematical model of Fig. 2.2 with the parameters:

G_m = 2390 μmho

G_c = 1920 μmho

G = 275 μmho

C_g = 1000 pf

C = 300 pf

Again the grid and plate current characteristics of Figs. 1.2 and 1.3 are assumed.

The contours of both the $\dot{E}$ and $\dot{E}_c$ surfaces are shown, and the

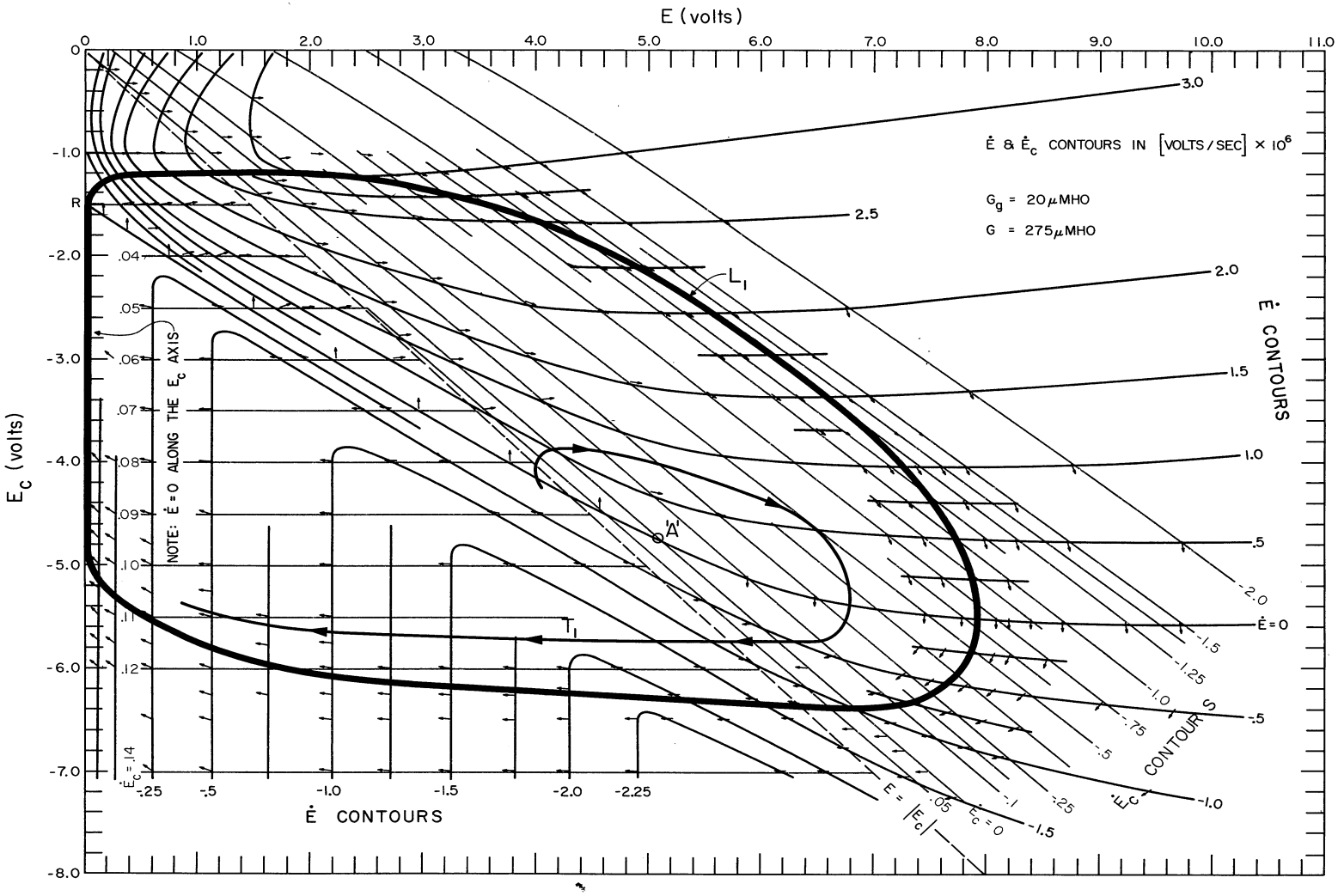

Fig. 4.3. (E, E_c)-plane diagram example of an (SLC-UE) configuration.

solution-path directions are indicated by vectors. In this case the (SLC-UE) configuration possesses one limit cycle, i.e., the limit cycle labeled L_1. An application of the stability criterion reveals that the equilibrium point A is now an unstable focus (note that the $\dot{E}_c = 0$ contour intersects the $\dot{E} = 0$ contour well to the left of the minimum E_c point). Thus, all initial conditions inside L_1 result in solutions which spiral out to L_1. It should be noted that all initial conditions outside L_1 also result in solutions spiralling to L_1. Therefore, after a short transient, such as T_1 in the figure, all initial conditions lead to operation on L_1; i.e., there is only one stable mode of operation.

Note that a part of the limit cycle L_1 appears to coincide with the E_c axis; however, this is not the case. If the region of the (E, E_c) plane in the neighborhood of the E_c axis were expanded it would be found that below the $\dot{E} = 0$ contour the limit cycle would be close to and approaching even closer to the E_c axis. This may be seen from Eq. 3.1 by noting that in this region $\sigma = \varphi = 0$ [Eq. 2.22 and Eq. 2.23], and thus

$$\dot{E} = - \frac{G}{2C} E \ ,$$

giving a solution $E(t)$ which decays exponentially toward zero. This decay continues until, on crossing the $\dot{E} = 0$ contour, $\dot{E}$ becomes positive and the limit cycle begins to depart from the E_c-axis. (A sketch of the behavior is shown in Fig. 4.4.) Therefore, it is always assumed that the limit cycle, L_1, does not touch the E_c axis. However, the minimum separation between L_1 and the E_c axis does determine whether L_1 corresponds to a squegging mode or an amplitude-modulated mode of oscillation. In order to make this distinction it is necessary to consider residual circuit noise.

When the limit cycle, L_1, is extremely close to the E_c axis for a relatively long time (it can be shown that the time necessary to traverse the limit cycle on its increasing E_c side is many times greater than the time required for its decreasing E_c side, cf., Fig. 2.3), as in Fig. 4.3, the resulting oscillation exhibits two important characteristics. First, since E is very close to zero for a relatively long time, the oscillation waveform is in the form of a train of RF pulses. Secondly, between pulses E becomes so small that residual circuit noise, which is not considered directly in the mathematical analysis of this report, becomes the dominant tank voltage, and a stochastic character is evidenced in the train of RF pulses. For example, there is small or no correlation between the pulse phases; also the time interval between pulses has some "jitter" associated with it.

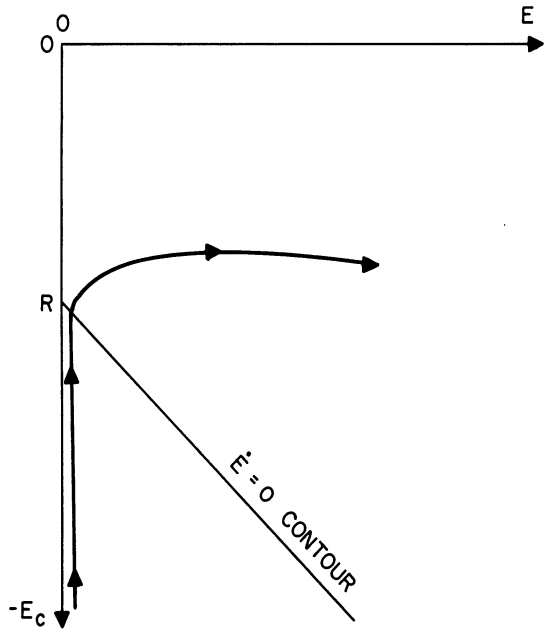

Fig. 4.4. Sketch of limit cycle in the neighborhood of the E_c-axis.

In this report, the limit cycle L_1 is said to be associated with a squegging mode of oscillation if the limit cycle comes so close to the E_c axis that there is zero (or, sometimes, just small) correlation between the phases pulse to pulse. Figure 4.3 illustrates such

a situation[1]. A typical grid-voltage waveform for a squegging mode of oscillation is shown in Fig. 4.5.

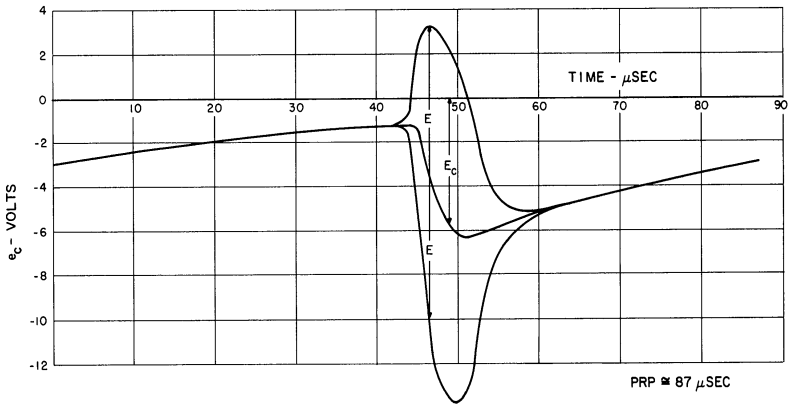

(a) Theoretical result.

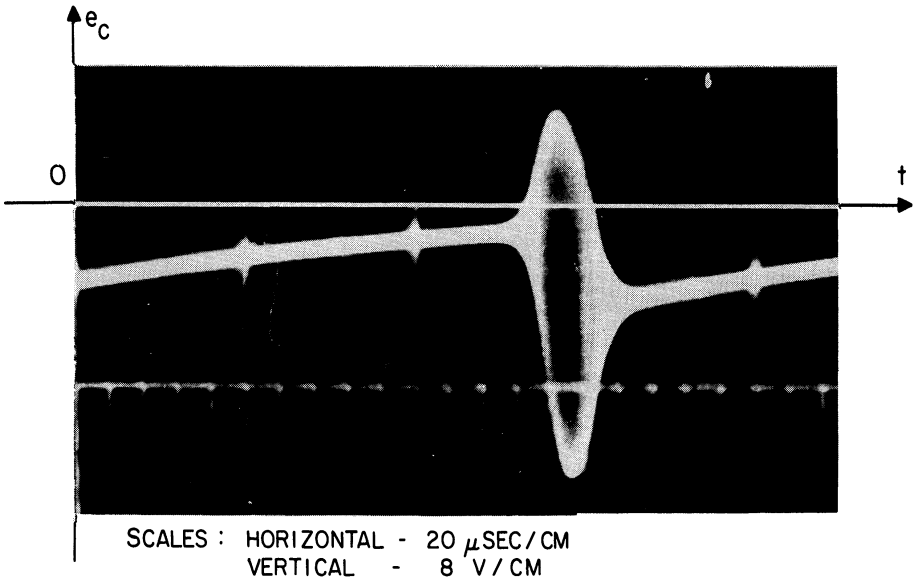

(b) Experimental result.

Fig. 4.5. Typical grid-voltage-waveform squegging mode.

[1] Actually it is not readily obvious whether some limit cycles are associated with squegging or amplitude-modulated modes of oscillation. However, in many cases a few simple calculations will make the determination easier. Since the limit cycle approaches the E_c axis in the region where

$$E < -(E_c - R),$$

no grid or plate current flows and linear circuit concepts may be applied. Thus in this region

$$E_c = E_{co}\, e^{-\frac{t}{R_g C_g}}$$

and

$$E = E_o\, e^{-\frac{G_t}{2C}t},$$

where E_o, E_{co} is any point on the limit cycle and in the specified region. An application of these equations to L_1 in Fig. 4.3 with $E_o = 0.1$ v and $E_{co} = -5$ v shows that in the time required for E_c to decay to a value of R (R = -1.5 v), E has decayed to approximately 9×10^{-23} v. Assuming that the circuit noise is at least as great as the thermal noise in the tank circuit, which is given by [Ref. 6]

$$\bar{e}^2 = \frac{kT}{C} = 13.3 \times 10^{-12}$$

it should be safe to assert that L_1 in Fig. 4.3 would be associated with a squegging oscillation.

The theoretical waveform in Fig. 4.5(a) was obtained from an application of the integration technique described in Section 4.2 to the limit cycle, L_1, in Fig. 4.3. The experimental result is an oscillograph of the grid waveform of an operating oscillator. Since the circuit parameters of the oscillator have been adjusted to correspond to those assumed in plotting Fig. 4.3, a comparison of Fig. 4.5(a) and (b) gives a check on the validity of the mathematical model.

If the limit cycle, L_1, does not come sufficiently close to the E_c axis for the noise to become important, the limit cycle is said to be associated with an amplitude-modulated mode of oscillation. A typical grid voltage waveform for an amplitude-modulated mode of oscillation is shown in Fig. 4.6. This figure is an oscillograph of an oscillator grid waveform.

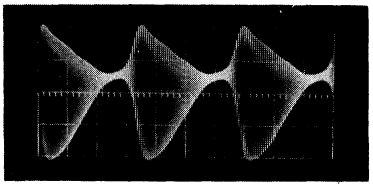

Fig. 4.6. Typical grid voltage waveform for an amplitude-modulated mode.

Obviously, if one wanted to build an oscillator which exhibited a limit cycle mode (i.e., either a squegging or an amplitude-modulated mode) the (SLC-UE) configuration with only one stable limit cycle would be the desirable phase-plane configuration.

4.5 Stable-Limit-Cycle Stable-Equilibrium-Point Phase-Plane Configuration [The(SLC-SE) Configuration]

In this case there are again only two equilibrium points: point A and the origin. The equilibrium point at the origin is unstable, and the one at point A is stable. Furthermore, there is at least one stable limit cycle encircling point A. Since A is stable, there must also

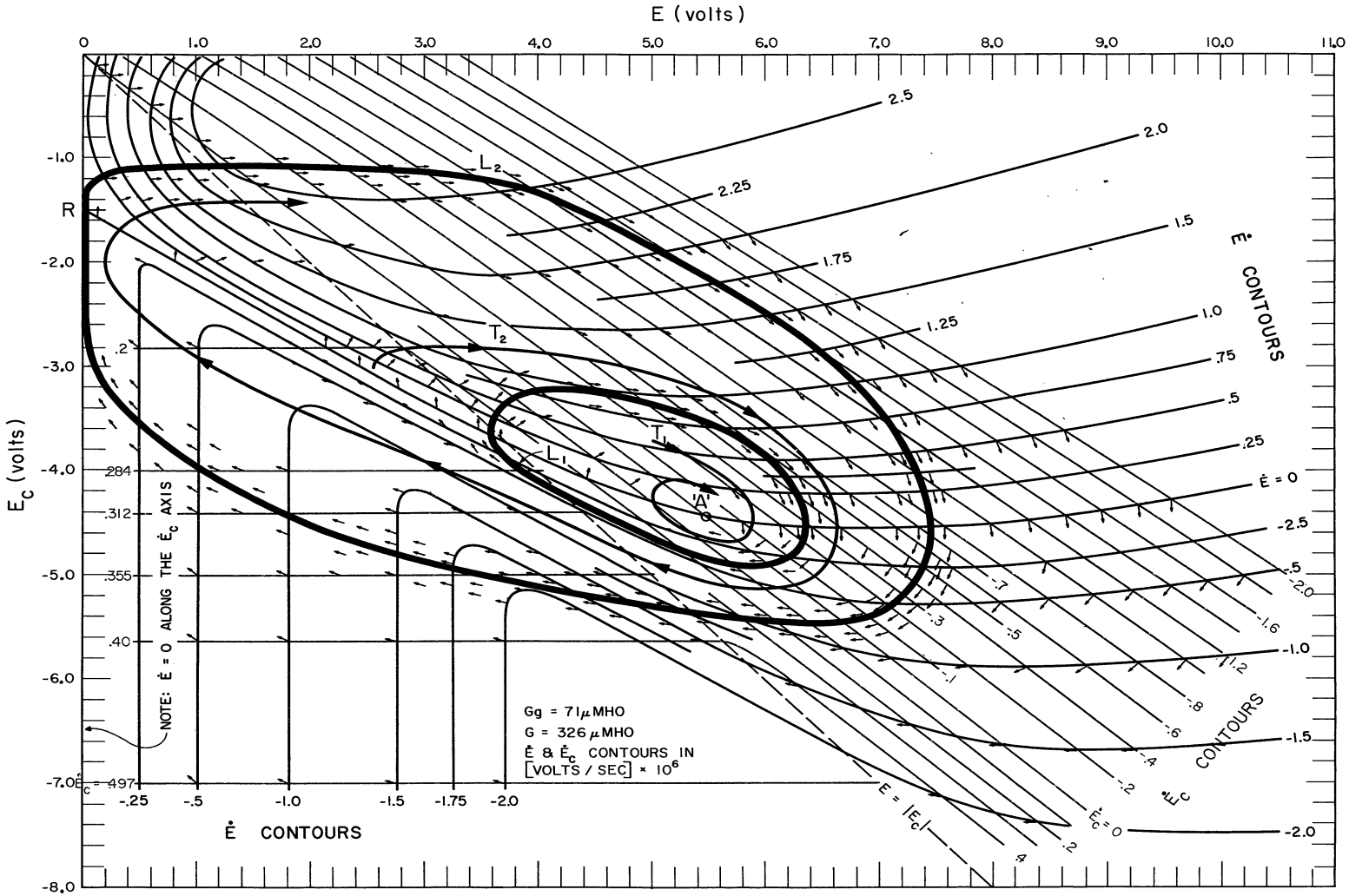

Fig. 4.7. (E, E_c)-plane diagram example of an (SLC-SE) configuration.

be an unstable limit cycle lying between the stable limit cycle and the point A. Therefore, all solution paths beginning inside of the unstable limit cycle converge to A, and a CW mode results; whereas, all solution paths beginning in the annulus between the stable and unstable limit cycles converge to the stable limit cycle and a squegging or amplitude-modulated mode results. The stable limit cycle may be enclosed by other limit cycles which are alternatingly unstable, stable, etc., but the outermost will be required to be stable. A typical example of an (SLE-SE) configuration is shown in Fig. 4.7. This figure presents the phase-plane configuration which is associated with an oscillator model whose circuit parameters are

$$G_m = 2390 \ \mu\text{mho}$$

$$G_c = 1920 \ \mu\text{mho}$$

$$G = 326 \ \mu\text{mho}$$

$$G_g = 1000 \ \text{pf}$$

$$C = 300 \ \text{pf} \ ,$$

and the characteristics of Figs. 1.2 and 1.3 are assumed.

The important feature of Fig. 4.7 is that for one set of oscillator parameters two modes of oscillation are possible. That is, this oscillator can operate either in a CW mode (point A) or in a limit cycle mode (limit cycle L_2)[1]. As can be seen from Fig. 4.7, the mode which is taken up depends upon the initial conditions. If the initial conditions are anywhere outside of the limit cycle L_2(e.g., in some small neighborhood of the origin), the solution path converges to L_2, and the limit cycle mode is taken up. If the initial conditions are anywhere in the annulus between L_1 and L_2 the solution also converges to the limit cycle

[1] In this case E has decayed to approximately 450 μ volts at point R (see footnote, page 43). In order to avoid an analysis of circuit noise at this point, the squegging versus amplitude-modulated question is by-passed, in this case, by use of the more general term.

L_2 following a transient path similar to T_2. On the other hand, if the initial conditions are inside the limit cycle L_1, then the solution converges to the equilibrium point A along a path such as T_1. One convenient method of adjusting the initial conditions of an experimental oscillator employs an external CW signal near the oscillator frequency. Roughly speaking, the operating point of the experimental oscillator may be "adjusted" to a desired region of the (E, E_c)-plane by the size and frequency of the external signal injected into the oscillator tank circuit. This procedure distorts the existing phase-plane configuration, but if the external signal is suddenly removed, the configuration returns to normal and the oscillator operating point returns to a location, on a limit cycle or at an equilibrium point, dictated by the adjusted position (initial condition) involved.

Figure 4.8 illustrates the grid-voltage waveform for the oscillator represented in Fig. 4.7 when operating on the limit cycle L_2. The theoretical results are obtained through an integration around the limit cycle L_2 by the method described in Section 4.2, while the experimental results are an oscillograph of the grid voltage of an experimental oscillator. Again, the parameters of the experimental oscillator have been adjusted to match those assumed in Fig. 4.7 and thus a comparison of (a) and (b) gives a check on the validity of the mathematical model.

Finally, note again that in an (SLC-SE) configuration the stable limit cycle may be associated with either an amplitude-modulated or a squegging mode of oscillation. Again this depends only on the closeness of approach of L_2 to the E_c axis. Thus, by proper selection of circuit parameters, either case may be obtained.

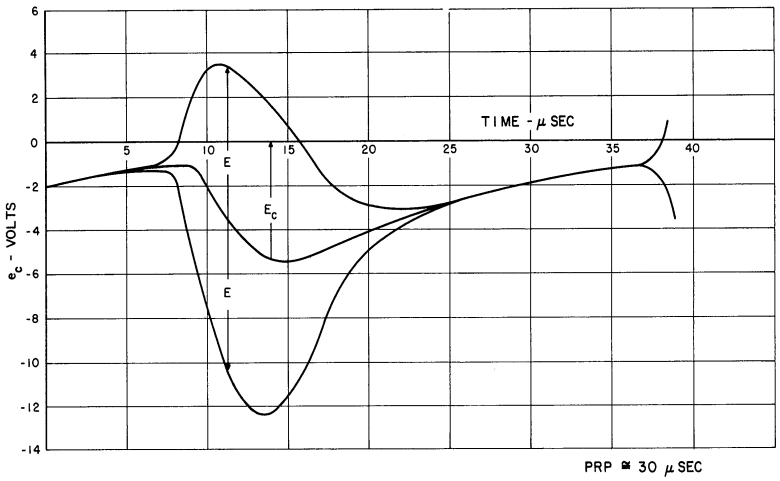

(a) Theoretical results.

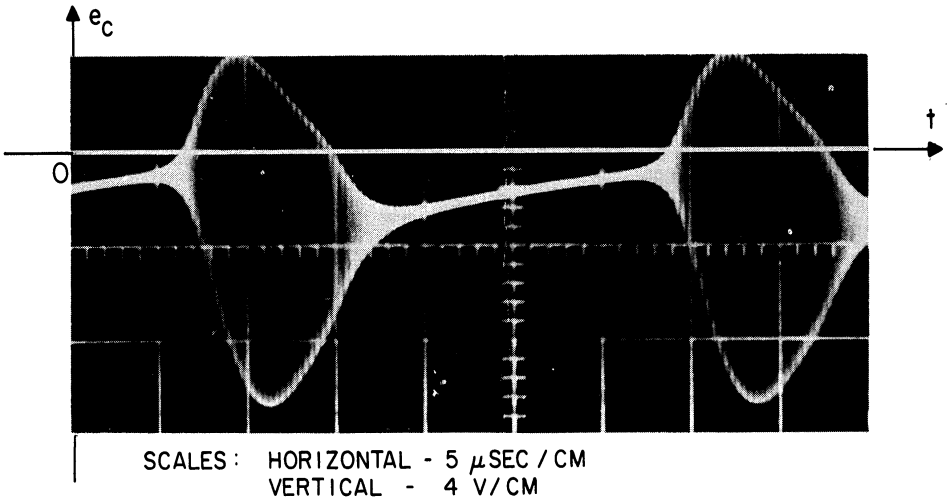

(b) Experimental results.

Fig. 4.8. Grid-voltage waveform for example in Section 4.5.

4.6 Effect of a Circuit Parameter Variation on the Phase-Plane Configuration

In the foregoing subsections the three classes of phase-plane configurations which are of interest here were defined and described. In this subsection, the phase plane and related concepts developed above are employed to predict the effect of circuit parameter variations on the behavior of a particular oscillator. In particular, a few examples

of the phase-plane configuration changing from one of the three classes to another are given. Throughout this subsection the circuit parameter that is considered to be variable is G_g. The effect of other parameter variations can be treated in a similar manner.

First, consider the effect upon the $\dot{E} = 0$ and $\dot{E}_c = 0$ contours of variations in G_g. Referring to Eq. 3.10 and recalling that $G = G_g + G'$, it follows that the $\dot{E} = 0$ contour is determined by

$$G' + G_g - G_m^{hf} + G_c^{hf} = 0 , \tag{4.7}$$

and the $\dot{E}_c = 0$ contour is determined by

$$G_g + G_c^{lf} = 0 . \tag{4.8}$$

Restricting attention to the specific grid and plate current characteristics considered in this report, Eqs. 3.6, 3.4, and 3.8 give

$$G_m^{hf} = \frac{G_m}{\pi} \left(\sigma - \frac{1}{2} \sin 2\sigma\right) , \tag{3.6}$$

$$G_c^{hf} = \frac{G_c}{\pi} \left(\varphi - \frac{1}{2} \sin 2\varphi\right) , \tag{3.4}$$

and

$$G_c^{lf} = \frac{G_c}{\pi} \left(\varphi + \frac{E}{E_c} \sin \varphi\right) . \tag{3.8}$$

Determination of the $\dot{E}_c = 0$ Contour:

Therefore, Eq. 4.8 becomes

$$G_g + \frac{G_c}{\pi} \left(\varphi + \frac{E}{E_c} \sin \varphi\right) = 0. \tag{4.9}$$

Recalling from Eq. 2.23 that

$$\varphi = \begin{cases} \cos^{-1}\left[\dfrac{-E_c}{E}\right] & \text{for } E \geq |E_c| , \\ 0 & \text{for } E \leq |E_c| ; \end{cases} \tag{2.23}$$

it follows that Eq. 4.9 becomes

$$\frac{G_g}{G_c} + \frac{1}{\pi}(\varphi - \tan\varphi) = 0. \qquad (4.10)$$

Equation 4.10 may now be solved for φ as a function of the ratio G_g/G_c, and this locus,

$$\varphi = \varphi\left[\frac{G_g}{G_c}\right] = \text{a constant},$$

is the $\dot{E}_c = 0$ contour. That this contour is a straight line passing through $E = E_c = 0$ with slope $(-\cos\varphi)$ may be seen from Eq. 2.23.

A plot of the function $1/\pi\ (\varphi - \tan\varphi)$ is shown in Fig. 4.9.

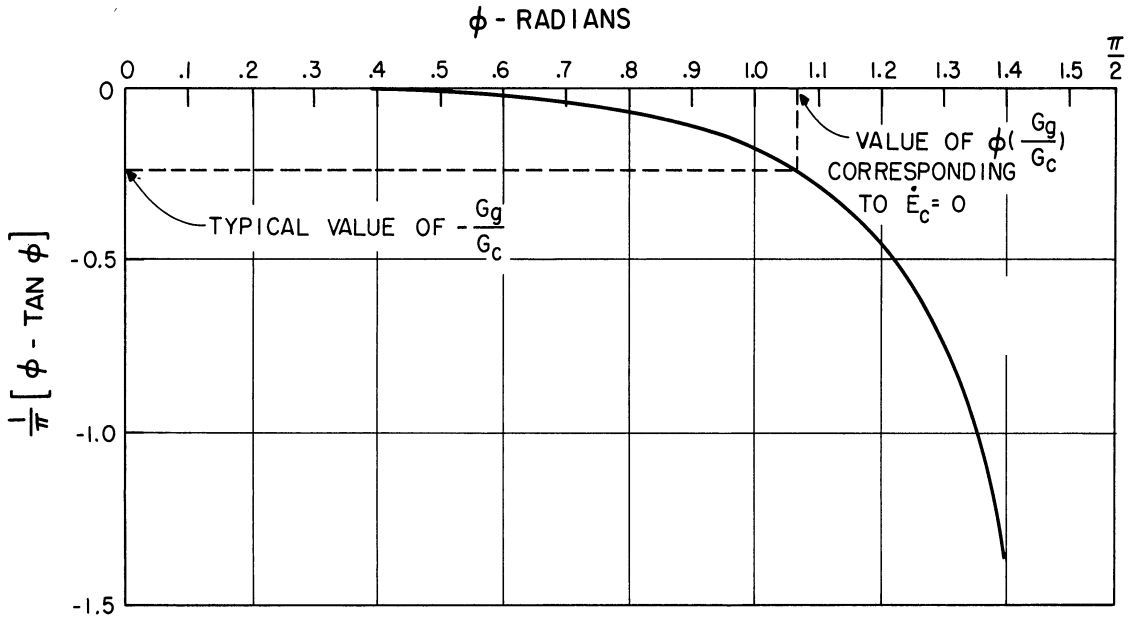

Fig. 4.9. Plot of $1/\pi\ [\varphi - \tan\varphi]$ versus φ.

As can be seen from Fig. 4.9, the φ which is a solution to Eq. 4.10 approaches 0 as $G_g/G_c \to 0$, and it approaches $\pi/2$ as $G_g/G_c \to \infty$. Thus the slope of the $E_c = 0$ contour varies from -1 to 0. Values of φ corresponding to values of G_g/G_c can be obtained from Eq. 4.10 through any of the standard techniques available for the solution of transcendental

equations. This solution could be plotted versus G_g/G_c; however, there is a more convenient way for presenting this information.

Since the angle φ is not easily measured directly in the (E, E_c) phase plane, it is more useful to transform the solution of Eq. 4.10 so that it can be immediately related to some angle in the phase plane. The angle, δ, selected for this purpose is shown in Fig. 4.10.

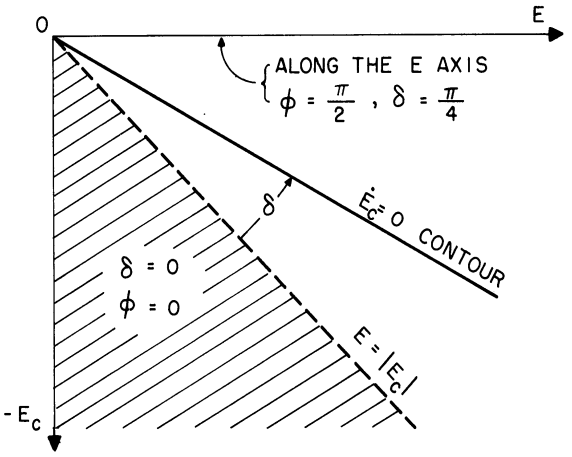

Fig. 4.10. Definition of angle δ.

Above the 45°-line in this figure, it can easily be shown by means of (2.23) and Fig. 4.10 that

$$\delta = \frac{\pi}{4} - \tan^{-1} [\cos \varphi]. \qquad (4.11)$$

Thus, if the solution of Eq. 4.10 is denoted $\varphi = \varphi(G_g/G_c)$, then the corresponding δ is given by

$$\delta \left(\frac{G_g}{G_c}\right) = \frac{\pi}{4} - \tan^{-1} \left[\cos \varphi\left(\frac{G_g}{G_c}\right)\right].$$

A plot of δ versus G_g/G_c is presented in Fig. 4.11. The main qualitative feature of Fig. 4.11 is that δ increases monotonically with G_g/G_c. In other words, the $\dot{E}_c = 0$ contour is a straight line through the origin which rotates from $\delta = 0^\circ$ to $\delta = 45^\circ$ as G_g/G_c goes from 0 to ∞.

Determination of the $\dot{E} = 0$ Contour:

Substituting (3.6) and (3.4) into (4.7) gives

$$G' + G_g - \frac{G_m}{\pi}\left(\sigma - \frac{1}{2}\sin 2\sigma\right) + \frac{G_c}{\pi}\left(\varphi - \frac{1}{2}\sin 2\varphi\right) = 0 . \qquad (4.12)$$

Clearly this expression does not admit to quite so straightforward a solution as Eq. 4.10. This is because, unlike the $\dot{E}_c = 0$ contour, the

$\dot{E} = 0$ contour is a function of both φ and σ.

Just as the locus φ = constant is a straight line through the origin, it is clear from Eq. 2.22 that the locus σ = constant is also a straight line through the point ($E = 0$, $E_c = R$) with slope ($-\cos\sigma$). Thus the relations described by (2.22) and (2.23) divide the E, E_c plane into regions as shown in Fig. 4.12. In the region where $\varphi = 0$ the $\dot{E} = 0$ contour must lie along one of the lines σ = constant, but in the remainder of the phase plane it will be a function of both σ and φ. That is, it is necessary to choose a value of φ and solve Eq. 4.12 for σ as a function of the parameters G, G_m, and G_c; thus,

$$\sigma = \sigma(\varphi; G_m, G_c, G) , \qquad (4.13)$$

where, again, $G = G_g + G'$.

As an aid in the determination of the $\dot{E} = 0$ contour the function $y = \frac{1}{\pi}\left[x - \frac{1}{2}\sin 2x\right]$ is plotted in Fig. 4.13. This figure can be used

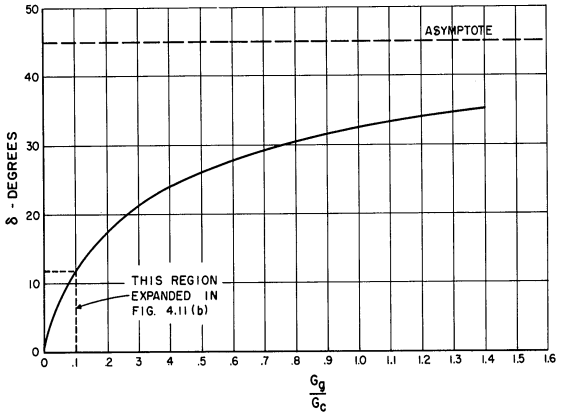

(a) Overall behavior.

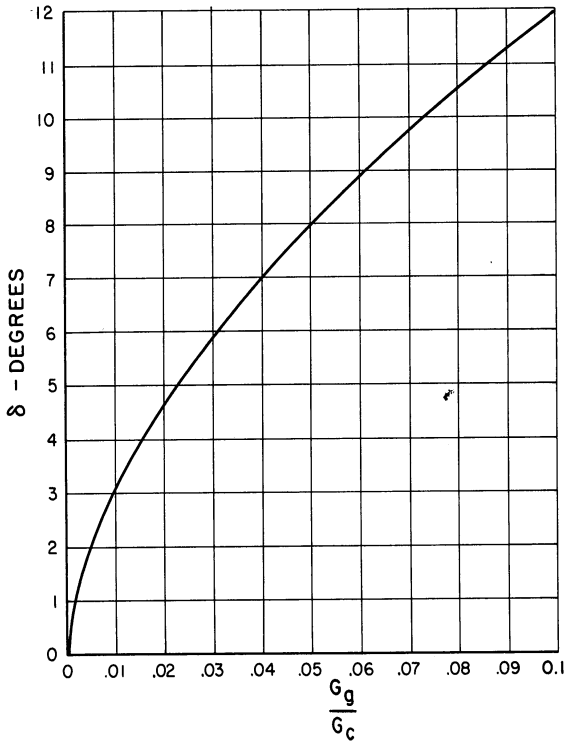

(b) Expansion of region of frequently encountered values of G_g/G_c.

Fig. 4.11. Angle δ of the $\dot{E}_c = 0$ contour in the phase plane vs G_g/G_c.

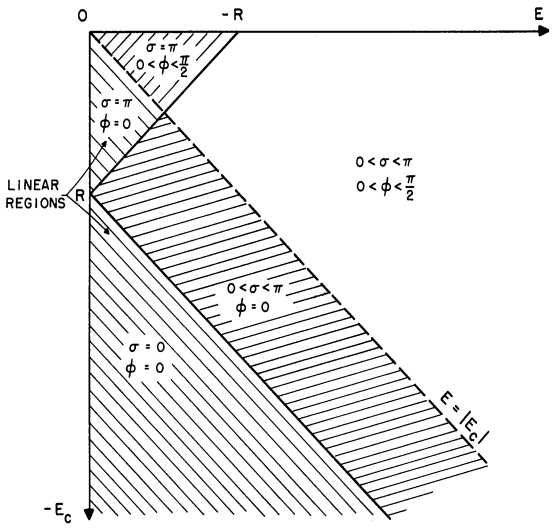

Fig. 4.12. Ranges of σ and φ in various regions of the (E, E_c)-plane.

in connection with either G_m^{hf} or G_c^{hf}.

The angle φ is related to an angle in the phase plane by Fig. 4.10 and Eq. 4.11. Following a similar procedure the angle σ can also be related to an angle in the phase plane, say η. Recall from Eq. 2.22 that

$$\sigma = \begin{cases} \cos^{-1}\left(\dfrac{R - E_c}{E}\right) & \text{for } E \geq |R - E_c| \,, \\ 0 & \text{for } E_c \leq R \text{ and } E < |R - E_c| \,, \text{ and} \\ \pi & \text{for } E_c \geq R \text{ and } E < |R - E_c| \,, \end{cases} \tag{2.22}$$

If the angle η is defined as shown in Fig. 4.14 it follows from Eq. 2.22 and Fig. 4.14 that

$$\eta = \frac{\pi}{4} - \tan^{-1}[\cos \sigma]. \tag{4.14}$$

Note the similarity between Eq. 4.14 and Eq. 4.11.

The foregoing equations aid in the determination and plotting of the $\dot{E} = 0$ contour. However, even with these aids this task is laborious. Therefore, Fig. 4.15 is presented in order that the qualitative

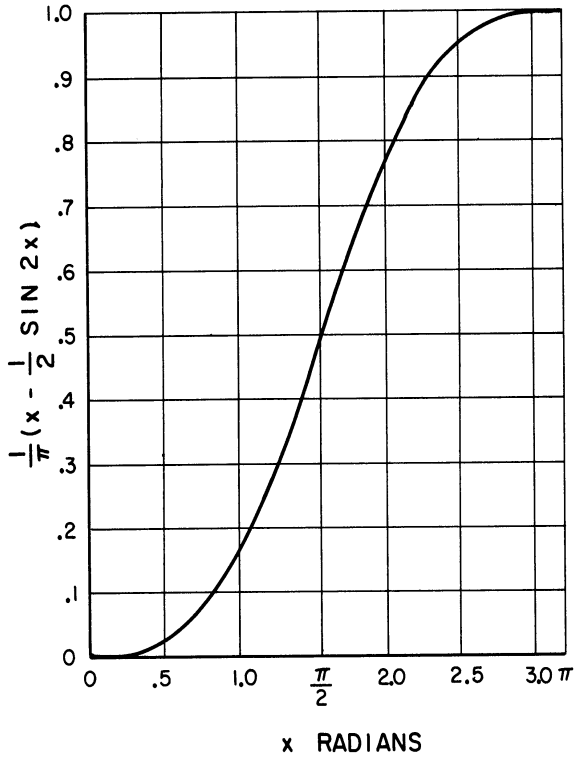

Fig. 4.13. Plot of $\frac{1}{\pi}(x - \frac{1}{2}\sin 2x)$ versus x.

effects of G_g variations can be appreciated. This figure shows the

$$\frac{G_m}{\pi}(\sigma - \frac{1}{2}\sin 2\sigma) - \frac{G_c}{\pi}(\varphi - \frac{1}{2}\sin 2\varphi)$$

surface above the (E, E_c)-plane for some representative values of G_m and G_c. In particular,

$$G_m = 2390 \text{ μmhos}$$

and

$$G_c = 1920 \text{ μmhos}.$$

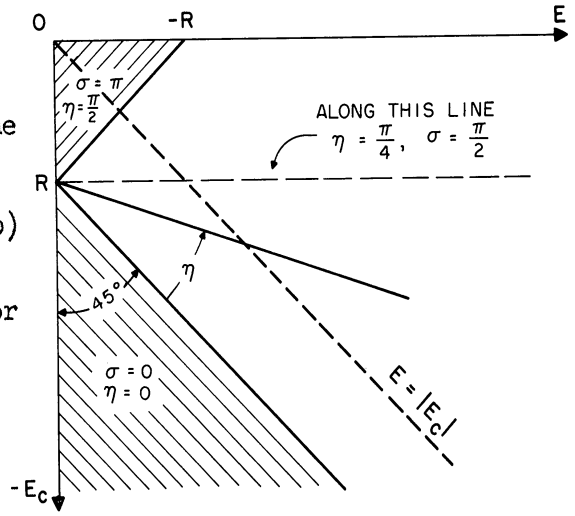

Fig. 4.14. Definition of the angle η.

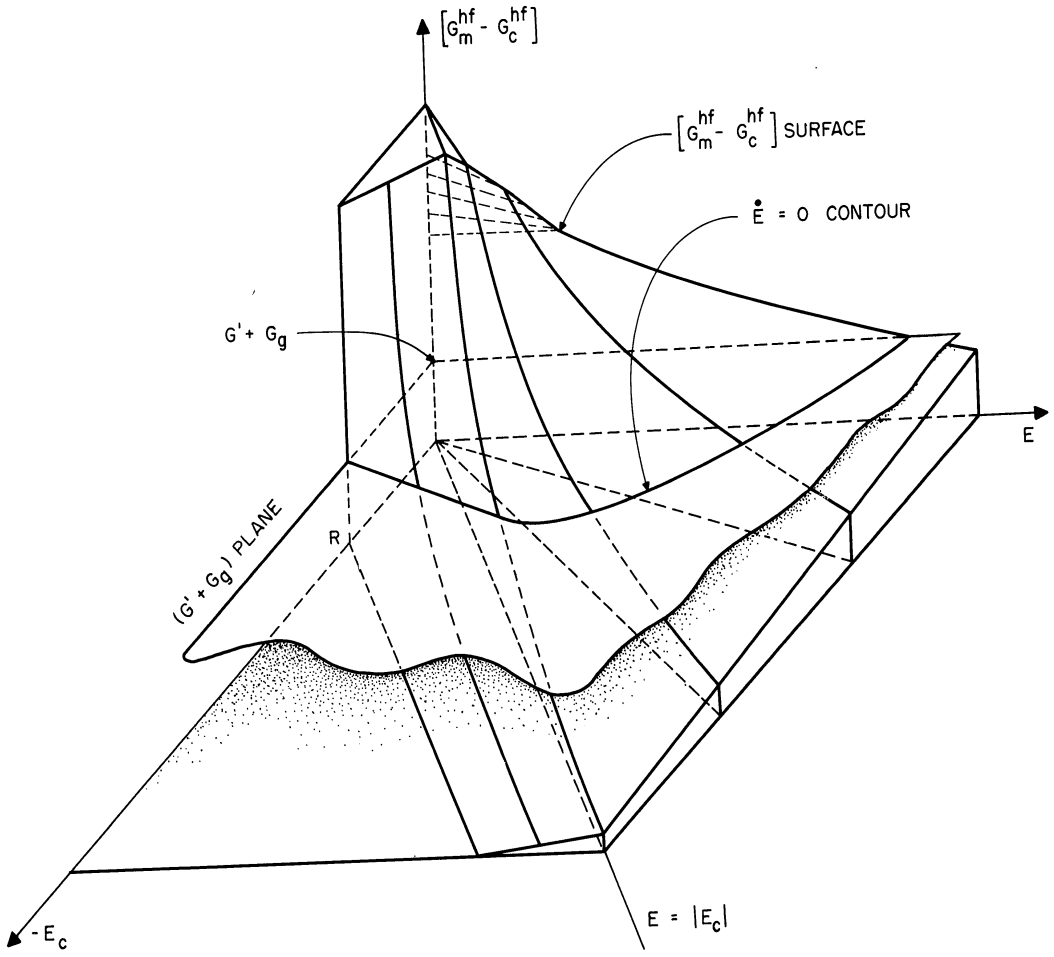

Fig. 4.15. $[G_m^{hf} - G_c^{hf}]$ surface over the (E, E_c) plane.

$G_m = 2390$ μmho $\qquad$ $G_c = 1920$ μmho

(These are the same values which are used in examples elsewhere in this report.) As shown in the figures, the $\dot{E} = 0$ contour is located on this surface at the level where

$$\frac{G_m}{\pi}\left(\sigma - \frac{1}{2}\sin 2\sigma\right) - \frac{G_c}{\pi}\left(\varphi - \frac{1}{2}\sin 2\varphi\right) = G' + G_g.$$

The significant feature shown in Fig. 4.15 is that as G_g increases the $\dot{E} = 0$ contour shrinks back toward the origin. Coupling this piece of information with the previously discussed behavior of the $\dot{E}_c = 0$ contour as a function of G_g, it follows that the variation of the equilibrium point location with G_g is similar to that in Fig. 4.16. Recalling the previous discussion in Subsection 4.3 of the stability of equilibrium point A, it can be seen that point A must become asymptotically stable-in-the-small for G_g larger than some minimum level since f_{1E} will become negative as the $\dot{E} = 0$ contour recedes and δ increases[1]. In fact, it can be seen from the figures of this section (and demonstrated analytically) that as G_g increases, $f_{1E} + f_{2E_c}$ decreases monotonically. Thus, an increase in G_g causes the equilibrium to move toward stability.

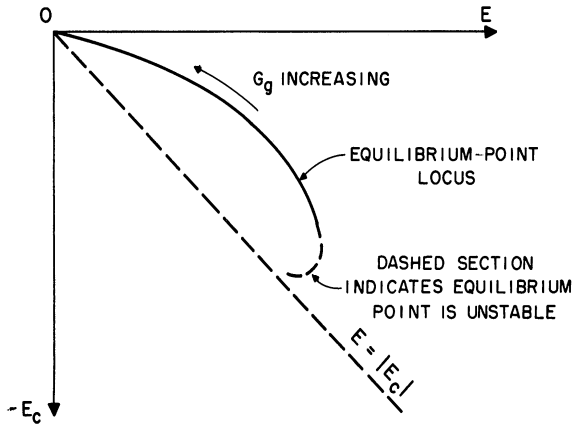

Fig. 4.16. Typical equilibrium point locus for various values of G_g.

Beyond the preceding statement there is very little of a general nature which can be said even if attention is restricted, as it has been in this subsection, to a particular pair of nonlinear charac-

[1] See Eq. 4.4(a), p. 36.

teristics for plate and grid current. On the other hand, there are two interesting patterns of dependence upon G_g that have been often observed both theoretically and experimentally which are readily explained in terms of phase-plane concepts.

The first pattern divides G_g values into three ranges. Starting at zero and slowly increasing G_g, the associated phase-plane configuration is (SLC-UE) until some critical value, $G_g = G_{g1}$, is reached. In this first range, $0 < G_g < G_{g1}$, the phase plane remains (SLC-UE) for all values of G_g but the finer details of the configuration do vary. In particular, as G_g increases, the stable limit cycle tends to decrease in size (cf., L_1 in Fig. 4.3, L_2 in Fig. 4.7) due to both the shrinkage of the $\dot{E} = 0$ contour and the increase in $\dot{E}_c$ in the linear region (Fig. 4.12).

As can be seen from either simple circuit considerations or a detailed application of the methods of Subsection 4.2, the increase in G_g and decrease in limit cycle size is accompanied by a decrease in pulse repetition period (PRP) of the limit cycle mode[1]. As the PRP decreases, the time available for E to decay between pulses is reduced. Thus the minimum value of E increases, and if the operation was originally in a squegging mode it tends toward amplitude modulation. However, it should be noted that the change from squegging to amplitude modulation is not accompanied by any noticeable alteration in the phase plane. A typical relation between PRP and G_g is sketched in Fig. 4.17.

When G_g increases past G_{g1} the real part of the characteristic roots ($f_{1E} + f_{2E_c}$) becomes negative and the equilibrium point becomes

---

[1]The term PRP is obviously derived from the true pulses noted in a squegging mode. In an amplitude-modulated mode this is more accurately described as the fundamental modulation frequency, however, the term PRP will still be used here.

stable. In this second range, $G_{g1} < G_g < G_{g2}$, the stable equilibrium point is encircled by both an inner, unstable limit cycle and an outer, stable limit cycle; thus, the (SLC-SE) configuration exists. Within this second range variations in G_g have two important effects on fine detail. As G_g increases, the stable limit cycle (and the PRP of any limit cycle mode) continuously decreases in size as it did in the first region. However, the unstable limit cycle, which formed around the equilibrium point when it became stable, is extremely small for G_g near G_{g1} and grows with G_g until it is almost coincident with the stable limit cycle for G_g near G_{g2}.

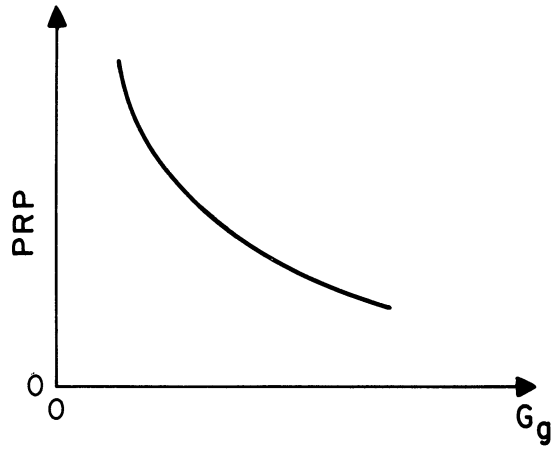

Fig. 4.17. Typical variation in PRP with G_g for $G_g < G_{g1}$.

As G_g increases past G_{g2} the stable and unstable limit cycles coalesce and disappear. In this third range, $G_g > G_{g2}$, the equilibrium point remains stable and the (PSLE) configuration exists. If G_g is decreased, the above sequence changes in the phase-plane configuration occur in reverse order. However the sequence of oscillation mode is altered. This will be discussed below. A complete picture of this first pattern including possible modes of oscillation in each of the three ranges is shown in Fig. 4.18.

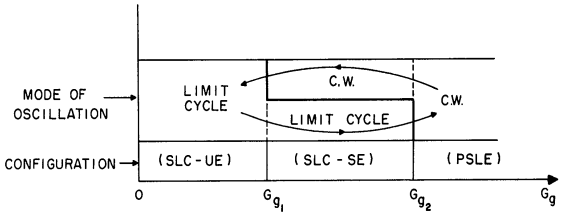

Fig. 4.18. Phase-plane configuration and possible oscillation modes versus G_g--first pattern.

An interesting consequence of the pattern portrayed in Fig. 4.18 is that for certain values of G_g (i.e., $G_{g1} < G_g < G_{g2}$) two stable modes of oscillation exist. Moreover, the pulse-repetition period (PRP) versus G_g exhibits a jump phenomenon. For example, starting at a small G_g which corresponds to an (SCL-UE) configuration the oscillator exhibits a limit cycle mode. As G_g is slowly increased and crosses the boundary G_{g1} between the (SLC-UE) and (SLC-SE) configurations the oscillator naturally remains in a limit cycle mode, although the CW mode associated with the stable equilibrium point A is now also possible. As G_g is further increased and crosses into the (PSLE) configuration region at G_{g2} the limit cycle ceases to exist, and the oscillator takes up a CW mode. If now G_g is slowly decreased and recrosses the boundary between the (PSLE) and (SLC-SE) configurations, the oscillator remains in the CW mode. As G_g is further decreased and crosses into the (SLC-UE) configuration region, the equilibrium point becomes unstable and a squegging mode is taken up. A sketch of the resulting PRP versus G_g behavior is shown in Fig. 4.19. The figure shows the hysteresis in PRP which is characteristic of this first pattern. The three sample phase-plane configurations shown in Figs. 4.2, 4.3, and 4.7 are from a system exhibiting this first pattern.

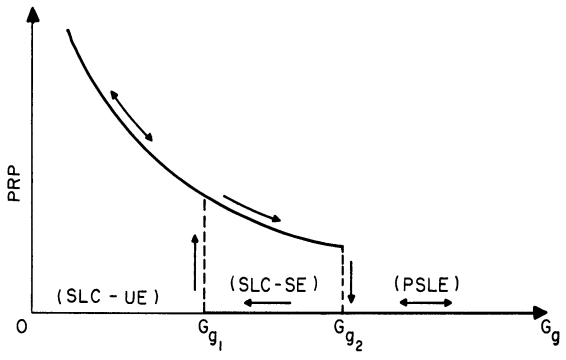

Fig. 4.19. Typical variation in PRP with G_g--first pattern. (PRP of zero corresponds to CW mode)

The second pattern divides G_g values into only two ranges. In this case the results are somewhat similar to the first pattern if it were found that $G_{g1} = G_{g2} = G_{g12}$; thus, the (SLC-SE) configuration and

the hysteresis would not occur. In the first range, $G_g < G_{g12}$, the (SLC-UE) configuration exists and only a limit cycle mode of oscillation may occur. As G_g is increased, inside this range, the limit cycle again grows smaller. However, in this pattern the stable limit cycle shrinks continuously until it is an extremely small curve surrounding the still unstable equilibrium point. As in the first pattern, the limit cycle shrinkage is accompanied by an increase in PRP and an increase in the minimum value of E between pulses. Thus, if the limit cycle mode was initially a squegging mode, the increase in G_g causes it to become an amplitude-modulated mode.

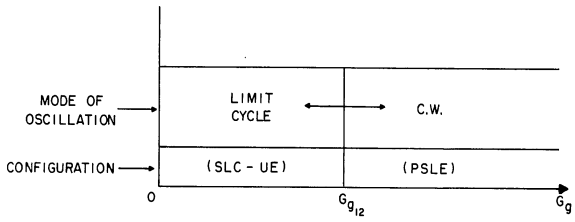

Fig. 4.20. Phase-plane configuration and possible oscillation mode versus G_g--second pattern.

In the second range G_g becomes greater than G_{g12}. As G_g increases through G_{g12} the limit cycle coalesces with the unstable equilibrium point leaving only a stable equilibrium point and a (PSLE) configuration for all $G_g > G_{g12}$. The foregoing is portrayed in Fig. 4.20. It is clear that since there is now no bistable configuration there will be no PRP hysteresis. The PRP versus G_g curve for the second pattern is shown in Fig. 4.21. In this pattern it is seen that there is also no PRP jump. Since the stable limit cycle decreases smoothly to the equilibrium point the PRP decreases smoothly to zero. Thus the oscillation mode becomes amplitude modu-

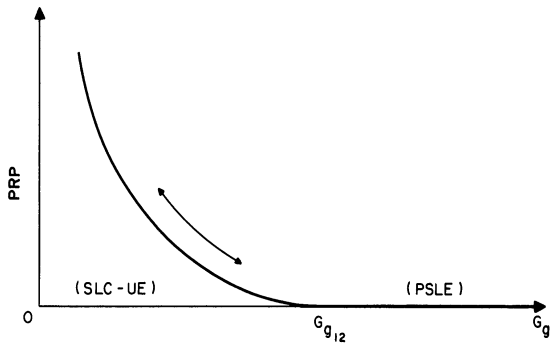

Fig. 4.21. Typical variation in PRP with G_g--second pattern. (PRP of zero corresponds to CW mode)

lated and the percent modulation of the waveform decreases with increasing G_g, becoming zero at G_{g12}. If the G_g is decreased the process is found to be completely reversible.

Examples of the (E, E_c)-plane patterns for this second pattern obtained experimentally are shown in Section 5. A sequence of analytically determined (E, E_c)-plane configurations such as Figs. 4.2, 4.3, and 4.7 for the first pattern are not given for the second. This sequence could, of course, be constructed by the same technique used previously.

5. EXPERIMENTAL RESULTS

5.1 Introduction

The foregoing sections have described the selection and analysis of a mathematical model for a grid leak biased oscillator. Since a mathematical model is useful only insofar as its solutions correspond to experimentally obtained results, a comparison must now be made between theoretically and experimentally obtained results. The experimental results will be compared with the theoretical results of Section 4 where specific grid and plate characteristics similar to those of an actual oscillator were assumed.

5.2 The Experimental Oscillator and Characteristics

Figure 5.1 shows the circuit of an oscillator which was employed in the experiments which are reported here. The parameters of this circuit were chosen so that they conform with the parameters assumed in the examples presented in Section 4. The true grid and plate current curves for the tube used are plotted in Fig. 5.2 for E_b = 200 volts and

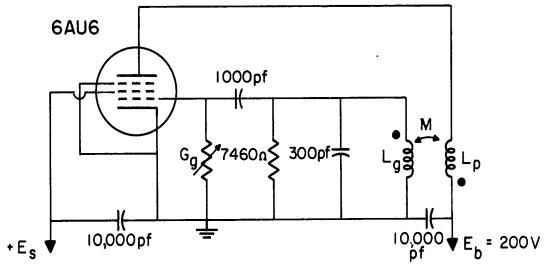

L_g = 10.6 μh

Q_g = 51 at 2.5 mc

L_p = 45.6 μh

Q_p = 76 at 2.5 mc

M = 5.1 μh

Fig. 5.1. Experimental oscillator circuit and parameters.

and E_s = 80 volts. From these curves it is clear that the piecewise linear approximations for the grid and plate characteristic mentioned in Section 1 are reasonable. In fact, the approximate characteristics fit the actual characteristics quite well when the constants of the approximate characteristics are chosen so that[1]

G_c = 1920 μmhos,

g_m = 4970 μmhos, and

R = -1.5 volts.

Then from definitions following Fig. 2.2

$$G_m = \frac{M}{L_g} g_m = 2390 \text{ μmhos.}$$

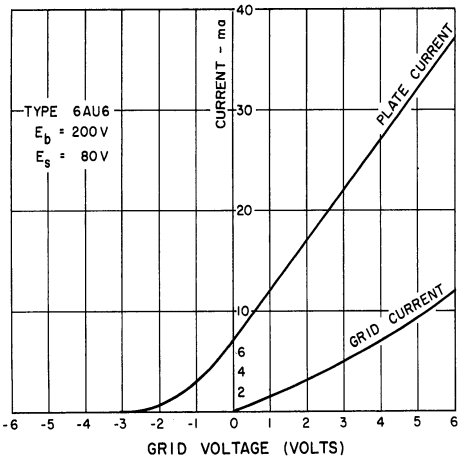

Fig. 5.2. Actual characteristerics of tube used in experimental oscillator.

5.3 Experimental Procedure for Display of Operating Path

The experimental setup shown in Fig. 5.3 was used to observe some of the (E, E_c)-plane operating paths (equivalently: solution paths) for the experimental oscillator. Those operating paths which could be

[1] Note that these are the values chosen for G_m, G_c, and R in the examples of Section 4.

observed with the aid of this setup correspond to stable equilibrium points and limit cycles in the model. In comparing these experimentally determined operating paths with those analytically predicted solutions in Section 3 it is found that there is good agreement between theory and experiment.

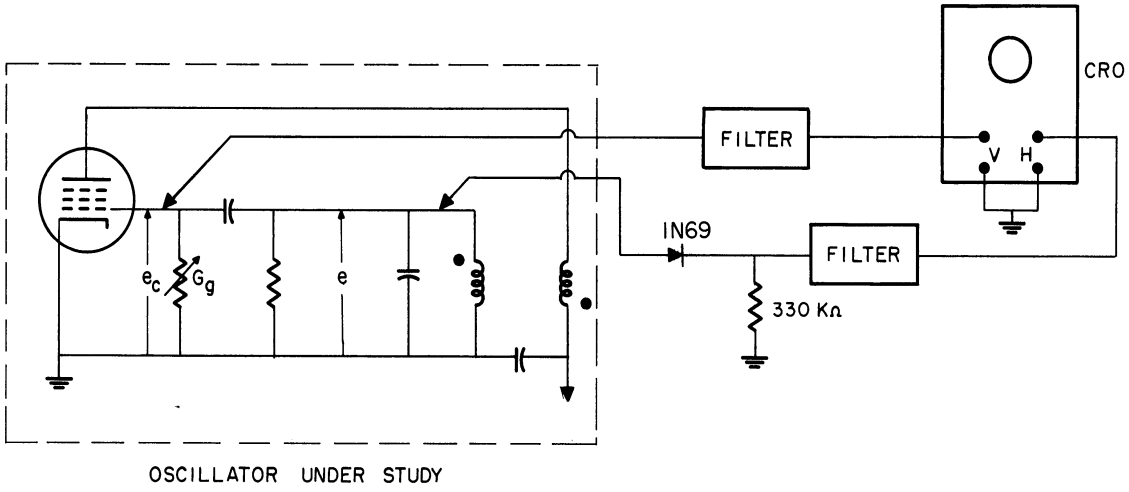

Fig. 5.3. Experimental system for display of oscillator operating path.

The operation of the experimental setup in Fig. 5.3 is quite simple. Voltages proportional to E and E_c are obtained from the oscillator and used to control the oscilloscope spot deflection. The only circuitry is the filter necessary to separate the RF from the E_c voltage and the detector and filter necessary to obtain the RF envelope voltage E. For the former a Hewlett-Packard AC-21A scope probe connected directly to the vertical amplifier of the HP-130A oscilloscope proved satisfactory. For the envelope detector a 1N69 diode, a 330 kΩ resistor, and a similar probe were used. The vertical deflection of the spot is then proportional to instantaneous values of E_c, and its horizontal position is proportional to the instantaneous value of E. Clearly, the resulting picture on the

oscilloscope face is just the phase plane with the operating path of a stable mode traced out upon it. Some representative operating paths will be shown in the next section.

5.4 Operation of the Experimental Oscillator

With the screen voltage, E_s, set to 80 volts the values of G_c and G_m mentioned above are obtained and the fixed parameters of the experimental oscillator correspond directly with the fixed parameters assumed in Section 4. Under these conditions, the operation of the experimental oscillator was observed for various values of G_g. At the outset of this experiment G_g was adjusted so that it was large enough to swamp out all oscillation. It was then slowly reduced until oscillation began. As expected from the considerations of Section 4 this was a CW mode of oscillation of small amplitude, E, and small associated grid bias, E_c. As G_g was further reduced the amplitude, E, increased and the grid bias, E_c, became a larger negative value. A CW mode was maintained until G_g reached 62.5 μmhos. At this point the CW mode suddenly disappeared and an amplitude-modulated mode appeared. Figure 5.4 is an oscillograph which shows the experimentally observed variation of the operating point (i.e.,

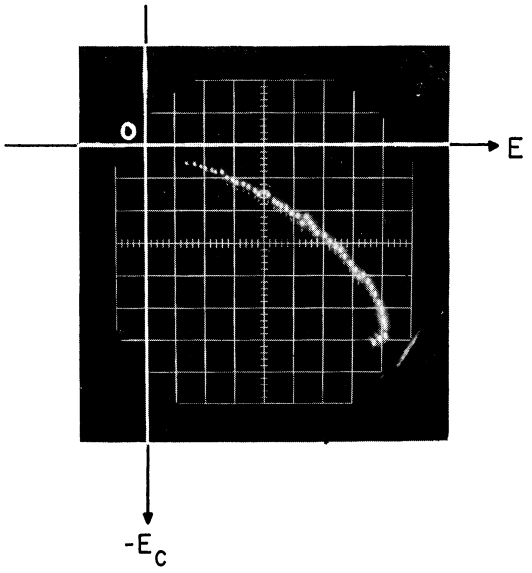

Fig. 5.4. Variation of CW operating point for 62.5 μmho < G_g < ∞. (Operating point moves up and to left as G_g increases.)

the equilibrium point A) as G_g was slowly reduced from the value at which oscillation started to the 62.5 μmhos, at which the stable CW mode ceased to exist. The character of this curve is just as expected from Section 4 and should be compared with Fig. 4.14.

At G_g = 143 μmhos the circuit parameters of the experimental oscillator were the same as those employed for Fig. 4.2. Oscillographs of the observed waveform and operating point are shown in Fig. 5.5. A

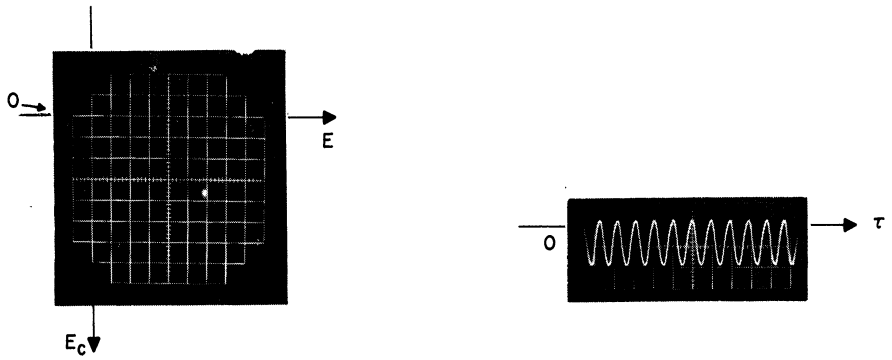

Fig. 5.5. Experimentally observed waveform and operating path for G_g = 143 μmhos.

comparison of the experimentally observed and the theoretically predicted location of the operating point follows.

	Predicted	Observed
E_c	-3.7 volts	-3.7 volts
E	5.3 volts	5.8 volts

Since the attempts to locate other stable modes of oscillation by varying the initial conditions were not successful, it is reasonable to

assume that the phase-plane configuration associated with the experimental oscillator was (PSLE) as predicted in Fig. 4.2.

As G_g was decreased below 62.5 μmhos the fundamental frequency of the modulation on the amplitude-modulated mode decreased; that is, the PRP increased. As G_g continued to decrease, the amplitude-modulated mode was transformed into a squegging mode. This transformation was marked by the appearance of PRP "jitter," one manifestation of the stochastic character of the squegging mode.

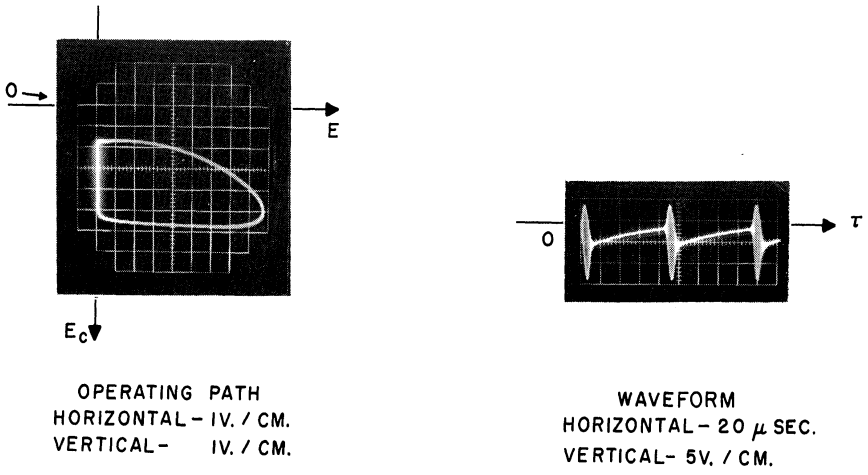

Fig. 5.6. Experimentally observed waveform and operating path for G_g = 20 μmhos.

At G_g = 20 μmhos the experimental circuit parameters were the same as those assumed for Fig. 4.3. The oscillographs in Fig. 5.6 show the experimentally observed waveform and operating path. The grid waveform of Fig. 5.6 should be compared with the predicted grid voltage waveform shown in Fig. 4.5(a). An overall comparison between the experimentally observed and the theoretically predicted results is given in the following tabulation.

	Predicted	Observed
PRP	87 μsec	85 μsec
Pulse Length[1]	7 μsec	7 μsec
Max E	8 volts	9 volts
Min E_c	-6.4 volts	-6 volts

Those numbers which are not directly observable in Fig. 4.3 (e.g., PRP) were calculated by means of the technique discussed in Subsection 4.2 (also see Fig. 4.5). Attempts to locate other stable modes of operation were again unsuccessful, and it seems reasonable to conclude that the squegging mode was the only stable mode of oscillation. Therefore, the phase-plane configuration of the experimental oscillator was (SLC-UE), as predicted by Fig. 4.3.

As G_g was slowly decreased below 20 μmhos there was no significant change in operation other than an increase in PRP. The minimum value of G_g, limited by leakage conductance of the circuit components (G_g removed), produces a normal, squegging-mode waveform with a very long PRP. This is again just as expected from Section 4.

G_g was then slowly increased from $G_g \ll 20$ μmhos. For values of G_g less than 62.5 μmhos the modes of oscillation for increasing G_g were found to be exactly the same as those observed when decreasing G_g. However, at $G_g = 62.5$ μmhos there was no sudden jump from the amplitude-modulated mode to the CW mode. Instead, the amplitude-modulated mode was maintained, and its PRP decreased as G_g continued to slowly increase. In this case, G_g reached 106 μmhos before the amplitude-modulated mode was transformed into a CW mode.

---

[1]Arbitrarily defined as the time during which the e_c pulse envelope extends above $e_c = 0$; i.e., $E > |E_c|$.

When G_g was increasing, the lowest PRP occurred for G_g slightly below 106 μmhos and was observed to be 20 μsec. However, for G_g decreasing, the lowest PRP occurred at 62.5 μmhos and was observed to be 35 μsec. A sketch which shows this hysteresis-like dependence of PRP upon G_g is presented in Fig. 5.7. A zero PRP in this figure corresponds to a CW mode of oscillation. Figure 5.7 should be compared with Fig. 4.19, and it should be noted that for 62.5 μmhos < G_g < 106 μmhos two stable modes of oscillation are possible. It is clear that for the above oscillator with E_s = 80 volts the G_{g1} and G_{g2} of Fig. 4.18 correspond to 62.5 μmhos and 106 μmhos, respectively. In this region G_g = 71 μmhos corresponds to the situation depicted by Fig. 4.7. The experimentally observed waveforms and operating paths are shown in Fig. 5.8. Here, as expected from Fig. 4.7, the two stable modes are an amplitude-modulated mode plus a CW mode. No other stable modes were found through variation of initial conditions and thus the occurrence of the (SLC-SE) configuration is confirmed. A comparison of experimentally observed and theoretically predicted results is given in the following table. The grid waveform in Fig. 5.8 should be compared with the theoretically determined waveform in Fig. 4.8(a). It should be noted that there are two stable operating paths observed (one is a point) but both do not occur simultaneously.

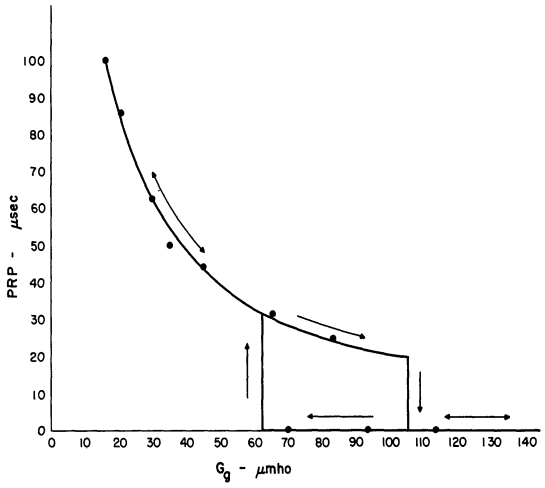

Fig. 5.7. PRP versus G_g for E_s = 80 volts.

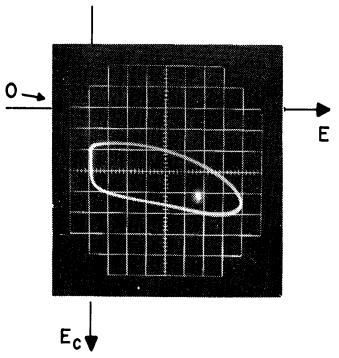

OPERATING PATHS
HORIZONTAL - 1V. / CM.
VERTICAL - 1V. / CM.

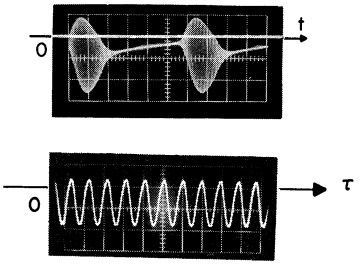

WAVEFORMS
VERTICAL - 5V. / CM ON (a) AND (b)
a) OPERATION ON OUTER PATH
HORIZONTAL - 5 μSEC / CM
b) OPERATION AT SINGULAR POINT.
HORIZONTAL - 0.4 μSEC. / CM.

Fig. 5.8. Experimentally observed waveforms and operating paths for G_g = 71 μmhos.

	Predicted	Observed
CW Mode		
E	5.4 volts	6 volts
E_c	-4.4 volts	-4 volts
Squegging Mode		
PRP	30 μsec	29 μsec
Pulse Length	7.5 μsec	8 μsec
Max E	7.5 volts	8 volts
Max E_c	-5.5 volts	-5 volts

As G_g is now increased beyond 106 μmhos the behavior occurring when G_g was decreased through this region is repeated in reverse order; i.e., the CW oscillation continues, and the values of E and E_c decrease

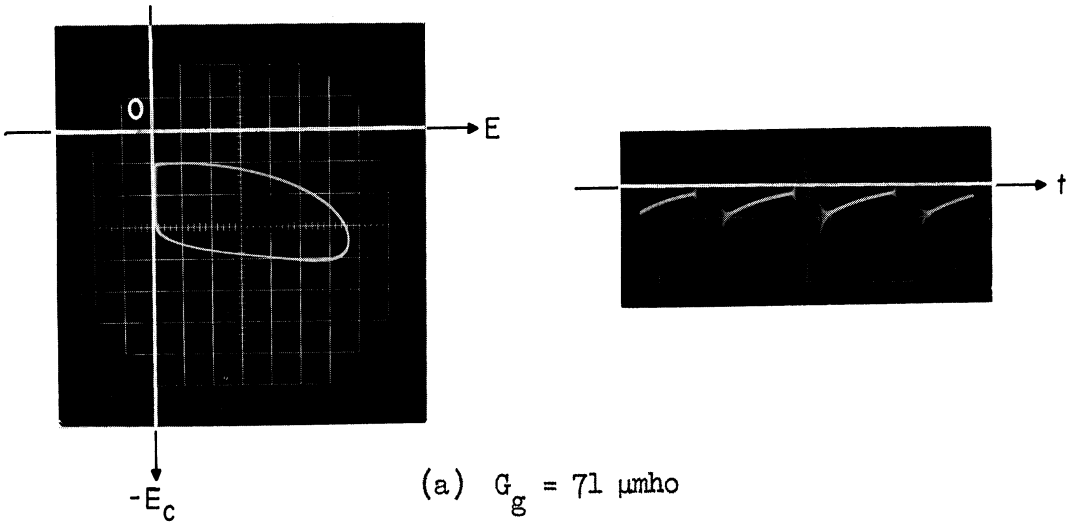

(a) G_g = 71 μmho

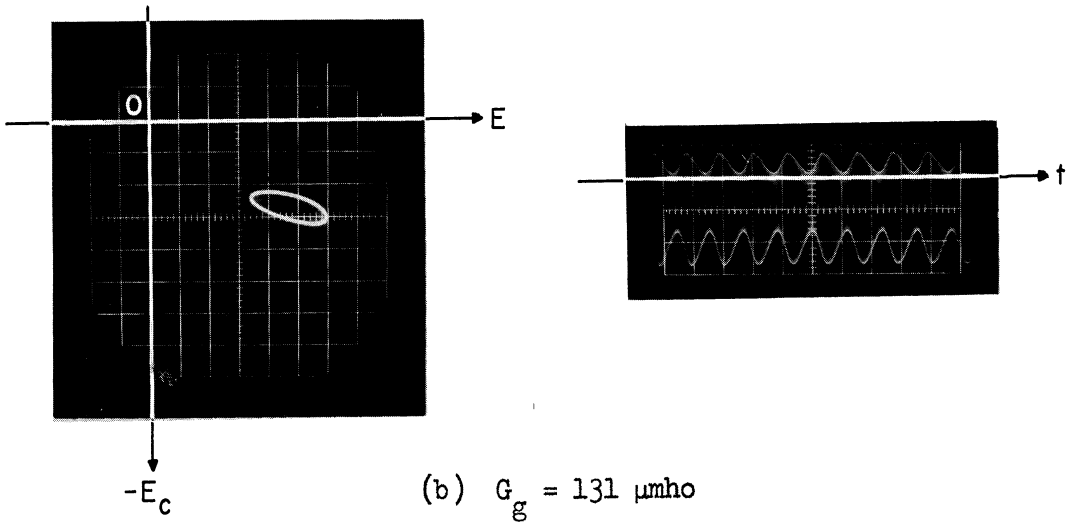

(b) G_g = 131 μmho

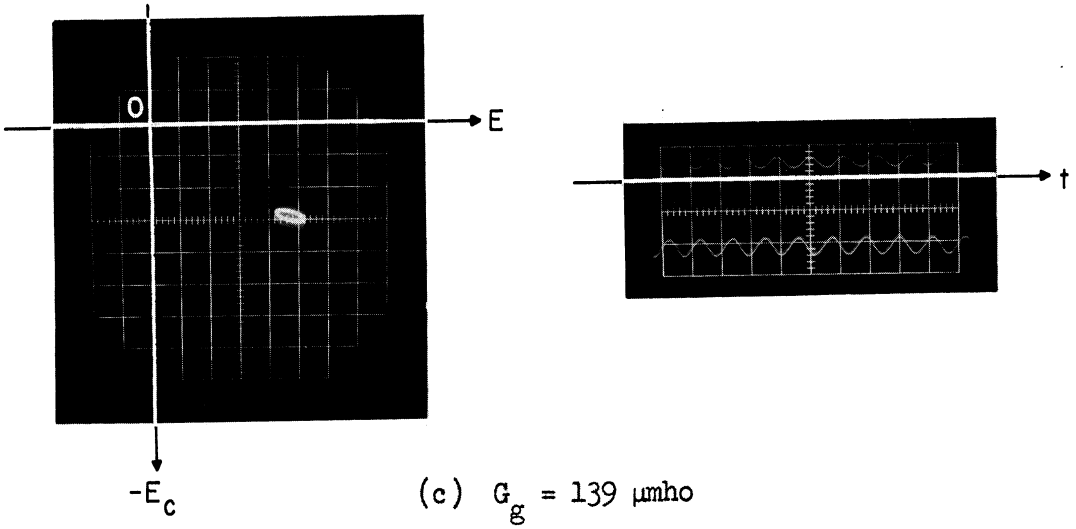

(c) G_g = 139 μmho

Fig. 5.9. Experimentally observed operating paths and waveforms. E_s = 170 volts.

Scales in these oscillographs are:

Operating Paths	Waveforms
Horizontal - 3 v/cm	Horizontal - 50 μsec/cm
Vertical - 3 v/cm	Vertical - 10 v/cm

as shown in Fig. 5.4.

The second pattern mentioned in Section 4 was observed with somewhat different circuit parameter values. As E_s was increased G_{g1} and G_{g2} approached each other in value until, when E_s = 170 volts, $G_{g1} = G_{g2} = G_{g12}$ = 141 μmho. At this value of E_s the multimode behavior was completely eliminated; i.e., only one stable mode of oscillation existed for each value of G_g. The change in waveform with G_g was then a smooth decrease in PRP and percent modulation as G_g increased, leading to a CW mode as the percent modulation approached zero. Fig. 5.9 shows waveforms and operating paths for several values of G_g for the oscillator shown in Fig. 5.1 with E_s = 170 volts.

Patterns other than those mentioned above have also been observed with the same oscillator. In some cases, it was found that more than one stable squegging or amplitude mode could be made to exist. None of the observed behaviors is inconsistent with the phase-plane analysis used here, and presumably appropriate phase planes could be constructed in all cases.

6. CONCLUSIONS

The early sections of this report describe a mathematical model for a class of oscillators. This class has been chosen so that it includes the common self-biased or grid-leak biased oscillators. However, the class has been left fairly general by allowing rather arbitrary choice of the two nonlinearities involved. The nonlinear differential equations describing this class of oscillators were then approximated by a new, more tractable, system of nonlinear differential equations. This latter system comprised the mathematical model for the class of oscil-

lators considered.

For a specific case corresponding to a certain subclass of self-biased oscillators, the model was subjected to detailed study using both analytical and phase-plane techniques. Besides the expected CW oscillation the model was found to predict several other modes of oscillation similar to those frequently observed in laboratory oscillators but not predicted by the commonly employed van der Pol mathematical model. Thus the new model is considered to be a more general description of oscillators than is provided by van der Pol's equation. From the phase-plane analysis of the model, it was possible to observe the relationships among the several modes of oscillation and their dependence on circuit parameters. The phase-plane analysis also permitted the prediction of somewhat unexpected phenomena which were later observed experimentally (e.g., bistable operation).

Having found a mathematical model it is desirable to have experimental verification of its validity. This is especially true where approximations of the Kryloff and Bogoliuboff types have been employed. Therefore, the experimental results of Section 5 are presented to corroborate the theoretical analysis by showing a qualitative and quantitative correspondence between theoretical and actual behavior of the oscillator. After comparing the predicted grid waveforms and operating paths with their experimental counterparts it seems quite reasonable to conclude that the model is valid, at least for the range of parameters considered in Section 5.

It is quite apparent that the complexity of the model limits its general utility, and that it is probably more useful in problems involving the minutiae of oscillator behavior or design (e.g., design

of oscillators with several stable states or specific waveforms). However, it has also been found valuable in gaining a thorough understanding of certain basic types of oscillators. The ability to consider rather arbitrary nonlinearities suggests that these advantages may be extended to the study of other devices where controlled oscillation is of interest, such as superregenerative detectors.

APPENDIX

In Section 4 of this report it was assumed that the equilibrium point A of Eq. 4.2 has an index of +1. The validity of this assumption, under certain reasonable restrictions, will now be shown. However, before proceeding, it is necessary to define the index and relate it to certain aspects of the phase-plane geometry. These aspects of the phase-plane geometry will then be employed to derive restrictions on the mathematical model which are sufficient to insure the +1 index.

Consider a system, S, of two first-order differential equations.

$$\begin{cases} \dot{E} = f_1(E, E_c) \\ \dot{E}_c = f_2(E, E_c) \ . \end{cases} \tag{A.1}$$

It will be assumed that both f_1 and f_2 are continous functions of E and E_c in the region $E \geq 0$, $E_c \leq 0$. At each point in the (E, E_c) phase-plane where f_1 and f_2 are not both zero the system, S, determines a unique direction

$$\theta = \tan^{-1} \frac{f_2(E, E_c)}{f_1(E, E_c)} \tag{A.2}$$

where:
$$\begin{cases} -\frac{\pi}{2} < \theta < \frac{\pi}{2} & \text{when } f_1 > 0 \\ \frac{\pi}{2} < \theta < \frac{3\pi}{2} & \text{when } f_1 < 0 \\ \theta = \frac{\pi}{2} & \text{when } f_1 = 0,\ f_2 > 0 \\ \theta = \frac{3\pi}{2} & \text{when } f_1 = 0,\ f_2 < 0 \end{cases}$$

Any simple closed curve, C, in the phase plane, not passing through an equilibrium point of S (i.e., a point where $f_1 = f_2 = 0$) has an index, N_c, given by[1]

$$N_c = \frac{1}{2\pi} \oint_C d\theta \tag{A.3}$$

[1] Kaplan, Op. cit.

The index N_c is obviously an integer since C is assumed closed. Note that the integral (A.3) is merely the rotation of the vector field associated with S accumulated along the curve C. A counterclockwise traversal of C is taken as positive.

The following facts are easily verified by simple geometric arguments. Complete proofs are available in the literature[1,2].

a. If C encloses no equilibrium points of S, then $N_c = 0$.

b. If C encloses a Node, Focus, or Center (the Node or Focus may be stable or unstable), then $N_c = +1$.

c. If C encloses a Saddle, then $N_c = -1$.

d. If C is a simple closed curve enclosing only one equilibrium point the value of N_c depends only on the type of equilibrium point enclosed and is independent of the size or shape of C.

In view of statement d. above, the index, I_A, of the equilibrium point A is defined as being equal to N_c when C encloses A and no other equilibrium point. That is,

$$I_A = N_c \mid \text{when C encloses A and only A.}$$

The equilibrium point A in the (E, E_c) plane occurs at the intersection of the $\dot{E} = 0$ and $\dot{E}_c = 0$ contours.[3] In the vicinity of this intersection the contours divide the plane into four regions. A typical intersection is shown in Fig. A.1.

---

[1] Kaplan, Op. cit.

[2] Minorsky, Op. cit.

[3] An equilibrium point can, by definition, occur only at a point of coincidence of the $\dot{E} = 0$ and $\dot{E}_c = 0$ contours. Any coincidence other than a crossing is structurally unstable and not of interest here.

In any one of the four regions $\dot{E}$ and $\dot{E}_c$ will have constant sign and the vector field angle, θ, will be restricted to a certain range. For instance, throughout one of the regions $\dot{E} > 0$ and $\dot{E}_c < 0$, and thus $3\pi/2 < \theta < 0$. Let the regions be denoted as

Region 1: where $\dot{E} > 0$, $\dot{E}_c > 0$

Region 2: where $\dot{E} < 0$, $\dot{E}_c > 0$

Region 3: where $\dot{E} < 0$, $\dot{E}_c < 0$

Region 4: where $\dot{E} > 0$, $\dot{E}_c < 0$

Assuming a coordinate system with E as the abcissa and E_c as the ordinate the angle θ must lie in quadrant 1 in Region 1, quadrant 2 in Region 2, etc.[1]

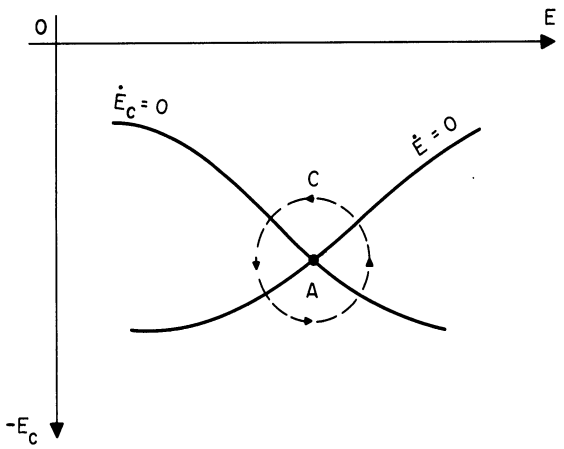

Fig. A.1. Regions in the vicinity of the equilibrium point A.

The question of the index of the equilibrium point A in Fig. A.1 is now reduced to one of determining the order of the regions encountered as the path C is traversed in a clockwise direction. An encounter order 1234 will make $I_A = +1$. Since the integration may start at any point on C the orders 2341, 3412, and 4123 will also give $I_A = +1$. On the other hand, an encounter order 4321, 3214, 2143, or 1432 will make $I_A = -1$. Orders such as 1324, 1423, etc., are not possible, since the $\dot{E} = 0$ and $\dot{E}_c = 0$ contours are assumed to cross at point A.

From the above statements it is clear that I_A will depend only on the arrangements of the regions in a neighborhood of A, and the existence of any arrangement of the proper order is sufficient to insure

[1] Here quadrants are defined in the usual sense; e.g., quadrant 1 is $0 \leq \theta < \pi/2$, etc., with $\theta = 0$ along the positive E axis.

that the equilibrium point has a +1 index. Thus, the index is independent of either the angle between the contours or the rotational orientation of the contours. In fact, as long as region 2 follows region 1 in counterclockwise rotation, the assumptions that the contours cross at the equilibrium point guarantees that the other regions will follow in order 3, 4 and the index will be +1. From the definitions of the regions 1 and 2 it may be stated that <u>if the point where counterclockwise traversal on curve C crosses the $\dot{E} = 0$ contour from $\dot{E} > 0$ to $\dot{E} < 0$ is in a region where $\dot{E}_c$ is positive, then the desired counterclockwise region order 1234 will be obtained.</u>

It is now necessary to relate the above result to conditions on the system of differential equations, S, and its associated phase-plane configuration. The following conditions on S will be shown <u>sufficient</u> to insure that the equilibrium point A has a +1 index.

a) There are at most two equilibrium points. The first, designated point A, must exist, may be located anywhere in the half-plane $E > 0$, and must be simple. The second, if it exists, must be located on the E_c-axis. Its location is designated point B.

b) In the half-plane $E > 0$, and $\dot{E} = 0$ and $\dot{E}_c = 0$ contours are simple[1] curves and do not terminate. The contours may have several branches but each branch may become nonsimple or terminate only on the E_c-axis.

c) $\dot{E} = 0$ along the E_c-axis.

d) The branch of the $\dot{E} = 0$ contour passing through the point A intersects the E_c-axis at only one point, which is desig-

[1] A curve is said to be simple if a small circle about any point of the curve intersects it at two and only two points.

nated point R. Furthermore, no other branch of the $\dot{E} = 0$ contour intersects this axis at R.

e) Throughout some sufficiently small neighborhood of R a point moving in the positive E_c direction along a line parallel to the E_c-axis crosses the $\dot{E} = 0$ contour once and only once and crosses from $\dot{E} < 0$ to $\dot{E} > 0$.

f) $B > R$ and $\dot{E}_c$ is positive along the portion of the E_c-axis where $E_c < B$. When there is only one equilibrium point, $\dot{E}_c > 0$ along the entire E_c-axis.

The above conditions are illustrated in Fig. A.2. Assuming these conditions, consider the branch of the $\dot{E} = 0$ contour passing through the equilibrium point A. Condition d) requires that this branch intersect the E_c-axis at some point R. Moreover, this branch cannot be closed on R since the $\dot{E}_c = 0$ contour would then be required to cross a closed curve at only one point [note that the $\dot{E}_c = 0$ contour cannot terminate at R since condition e) requires $S > R$]. Therefore, there is a unique path from R into the region $E > 0$ along the branch of the $\dot{E} = 0$ contour passing through point A, and condition e) shows that in moving out (from R) along this branch the region where $\dot{E} > 0$ will always be to

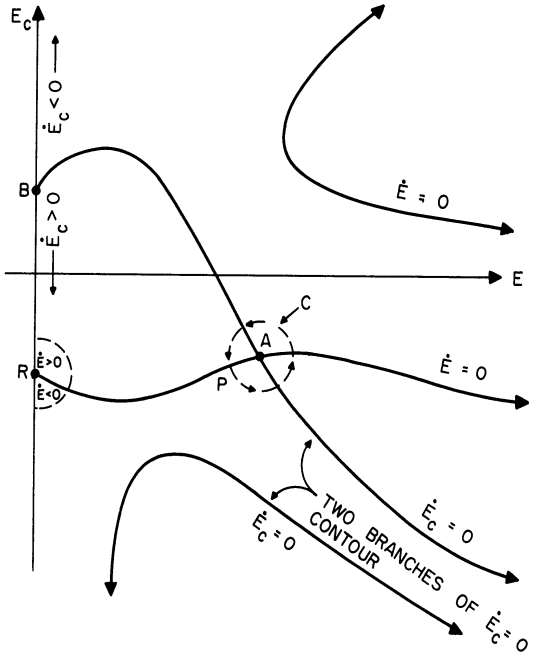

Fig. A.2. Phase-plane relations leading to $I_A = +1$.

the left. Now consider a small circle, C, drawn about the equilibrium point A as shown in Fig. A.2. This circle intersects the $\dot{E} = 0$ contour at only two points and at one of these points counterclockwise traversal of C crosses the contour from $\dot{E} > 0$ to $\dot{E} < 0$. This point will be called P. Since a counterclockwise traversal of the circle C must cross the $\dot{E} = 0$ contour from left to right at P, the point P must lie on the contour between R and A. If it can now be shown that $\dot{E}_c > 0$ at P, an index of +1 for point A will be assured. To show this, note that the $\dot{E}_c = 0$ contour divides the half-plane $E > 0$ into two or more regions. From condition f) it is seen that point R must lie in a region where $\dot{E}_c > 0$. Since the $\dot{E}_c = 0$ contour cannot cross the $\dot{E} = 0$ contour between points R and A, the point P must also lie in a region where $\dot{E}_c > 0$, and I_A must be +1.

The above proof can easily be extended to the case where $R > B$ by changing the location of the $\dot{E} > 0$ region. The point P will then fall beyond point A, and the rest follows in a simple fashion.

Although the above conditions on the system S are sufficient to insure that the equilibrium point A has an index of +1, they are not necessary and have been chosen mainly for ease of application. Thus these conditions may, in some cases, be too restrictive, and where they are not met, the earlier conditions on the regions surrounding the equilibrium point or the sign of $\dot{E}_c$ at point P might still be employed.

REFERENCES

1. Stoker, J. J., Nonlinear Vibrations, New York: Interscience Publishers, Inc., 1950.

2. N. Kryloff and N. Boboliuboff, Introduction to Nonlinear Mechanics, Princeton University Press, Princeton, N. J., 1943.

3. W. J. Cunningham, Introduction to Nonlinear Analysis, McGraw-Hill, New York, N. Y., 1958.

4. Kaplan, Ordinary Differential Equations, Addison-Weslye, Reading, Mass., 1958.

5. N. Minorsky, Introduction to Nonlinear Mechanics, Edwards Bros., Ann Arbor, Mich., 1947.

6. J. L. Lawson and G. E. Uhlenbeck, Threshold Signals, Radiation Laboratory Series, Vol. 24, McGraw-Hill, New York, 1950.

DISTRIBUTION LIST

Copy No.	
1-2	Commanding Officer, U.S. Army Signal Research and Development Laboratory, Fort Monmouth, New Jersey, ATTN: Senior Scientist, Countermeasures Division
3	Commanding General, U.S. Army Electronic Proving Ground, Fort Huachuca, Arizona, ATTN: Director, Electronic Warfare Department
4	Chief, Research and Development Division, Office of the Chief Signal Officer, Department of the Army, Washington 25, D. C., ATTN: SIGEB
5	Commanding Officer, Signal Corps Electronics Research Unit, 9560th USASRU, P. O. Box 205, Mountain View, California
6	U.S. Atomic Energy Commission, 1901 Constitution Avenue, N.W., Washington 25, D.C., ATTN: Chief Librarian
7	Director, Central Intelligence Agency, 2430 E Street, N.W., Washington 25, D.C., ATTN: OCD
8	Signal Corps Liaison Officer, Lincoln Laboratory, Box 73, Lexington 73, Massachusetts, ATTN: Col. Clinton W. Janes
9-18	Commander, Armed Services Technical Information Agency, Arlington Hall Station, Arlington 12, Virginia
19	Commander, Air Research and Development Command, Andrews Air Force Base, Washington 25, D.C., ATTN: RDTC
20	Directorate of Research and Development, USAF, Washington 25, D.C., ATTN: Chief, Electronic Division
21-22	Commander, Wright Air Development Center, Wright Patterson Air Force Base, Ohio, ATTN: WCOSI-3
23	Commander, Wright Air Development Center, Wright-Patterson Air Force Base, Ohio, ATTN: WCLGL-7
24	Commander, Air Force Cambridge Research Center, L. G. Hanscom Field, Bedford, Massachusetts, ATTN: CROTLR-2
25	Commander, Rome Air Development Center, Griffiss Air Force Base, New York, ATTN: RCSSLD
26	Commander, Air Proving Ground Center, ATTN: Adj/Technical Report Branch, Eglin Air Force Base, Florida
27	Commander, Special Weapons Center, Kirtland Air Force Base, Albuquerque, New Mexico
28	Chief, Bureau of Naval Weapons, Code RRRE, Department of the Navy, Washington 25, D.C.
29	Chief of Naval Operations, EW Systems Branch, OP-35, Department of the Navy, Washington 25, D.C.
30	Chief, Bureau of Ships, Code 691C, Department of the Navy, Washington 25, D.C.
31	Chief, Bureau of Ships, Code 684, Department of the Navy, Washington 25, D.C.
32	Chief, Bureau of Naval Weapons, Code RAAV-33, Department of the Navy, Washington 25, D.C.
33	Commander, Naval Ordnance Test Station, Inyokern China Lake, California, ATTN: Test Director-Code 30
34	Director, Naval Research Laboratory, Countermeasures Branch, Code 5430, Washington 25, D.C.
35	Director, Naval Research Laboratory, Washington 25, D.C., ATTN: Code 2021
36	Director, Air University Library, Maxwell Air Force Base, Alabama, ATTN: CR-4987
37	Commanding Officer-Director, U.S. Naval Electronic Laboratory, San Diego 52, California
38	Office of the Chief of Ordnance, Department of the Army, Washington 25, D.C., ATTN: ORDTU
39	Chief, West Coast Office, U.S. Army Signal Research and Development Laboratory, Bldg. 6, 75 S. Grand Avenue, Pasadena 2, California
40	Commanding Officer, U.S. Naval Ordnance Laboratory, Silver Springs 19, Maryland
41-42	Chief, U.S. Army Security Agency, Arlington Hall Station, Arlington 12, Virginia, ATTN: LADEV
43	President, U.S. Army Defense Board, Headquarters, Fort Bliss, Texas
44	President, U.S. Army Airborne and Electronics Board, Fort Bragg, North Carolina
45	U.S. Army Antiaircraft Artillery and Guided Missile School, Fort Bliss, Texas
46	Commander, USAF Security Service, San Antonio, Texas, ATTN: CLR
47	Chief, Naval Research, Department of the Navy, Washington, 25, D.C., ATTN: Code 93
48	Commanding Officer, U.S. Army Security Agency, Operations Center, Fort Huachuca, Arizona
49	President, U.S. Army Security Agency Board, Arlington Hall Station, Arlington 12, Virginia

Copy No.	
50	Operations Research Office, Johns Hopkins University, 6935 Arlington Road, Bethesda 14, Maryland, ATTN: U.S. Army Liaison Officer.
51	The Johns Hopkins University, Radiation Laboratory, 1315 St. Paul Street, Baltimore 2, Maryland, ATTN: Librarian
52	Stanford Electronics Laboratories, Stanford University, Stanford, California, ATTEN: Applied Electronics Laboratory Document Library
53	HRB-Singer, Inc., Science Park, State College, Pennsylvania, ATTN: R. A. Evans, Manager, Technical Information Center
54	ITT Laboratories, 500 Washington Avenue, Nutley 10, New Jersey, ATTN: Mr. L. A. DeRosa, Div. R-15 Lab.
55	The Rand Corporation, 1700 Main Street, Santa Monica, California, ATTN: Dr. J. L. Hult
56	Stanford Electronics Laboratories, Stanford University, Stanford, California, ATTN: Dr. R. C. Cumming
57	Willow Run Laboratories, The University of Michigan, P. O. Box 2008, Ann Arbor, Michigan, ATTN: Dr. Boyd
58	Stanford Research Institute, Menlo Park, California, ATTN: Dr. Cohn
59-60	Commanding Officer, U.S. Army Signal Missile Support Agency, White Sands Missile Range, New Mexico, ATTN: SIGWS-EW and SIGWS-FC
61	Commanding Officer, U.S. Naval Air Development Center, Johnsville, Pennsylvania, ATTN: Naval Air Development Center Library
62	Commanding Officer, U. S. Army Signal Research and Development Laboratory, Fort Monmouth, New Jersey, ATTN: U. S. Marine Corps Liaison Office, Code AO-4C
63	President, U.S. Army Signal Board, Fort Monmouth, New Jersey
64-73	Commanding Officer, U.S. Army Signal Research and Development Laboratory, Fort Monmouth, New Jersey ATTN: 1 Copy-Director of Research 1 Copy-Technical Documents Center ADT/E 1 Copy-Chief, Countermeasures Systems Branch, Countermeasures Division 1 Copy-Chief, Detection and Location Branch, Countermeasures Division 1 Copy-Chief, Jamming and Deception Branch, Countermeasures Division 1 Copy-File Unit No. 2, Mail and Records, Countermeasures Division 1 Copy-Chief, Interference Reduction Branch, Electromagnetic Environment Division 3 Copies-Chief, Security Division (for retransmittal to BJSM)
74	Director, National Security Agency, Fort George G. Meade, Maryland, ATTN: TEC
75	Dr. H. W. Farris, Director, Cooley Electronics Laboratory, Electrical Engineering Department, University of Michigan, Ann Arbor, Michigan
76-79	Cooley Electronics Laboratory Project File, Electrical Engineering Department, University of Michigan Research, Ann Arbor, Michigan
100	Project File, Office of Research Administration, Ann Arbor, Michigan

Above distribution is effected by Countermeasures Division, Surveillance Department, USASRDL, Evans Area, Belmar, New Jersey. For further information contact Mr. I. O. Myers, Senior Scientist, Telephone 59-61252 (area code 201)